JOURNAL OF GEOPHYSICAL RESEARCH, VOL. 104, NO. B5, PAGES 10,883–10,902, MAY 10, 1999

Contribution of ductile flow to exhumation of low-temperature, high-pressure metamorphic rocks: San Juan-Cascade nappes, NW Washington State

Jeffrey G. Feehan and Mark T. Brandon

Department of Geology and Geophysics, Yale University, New Haven, Connecticut

Abstract. The San Juan-Cascade (SJC) nappes were subducted to a depth of ~18 km, metamorphosed under low-temperature, high-pressure conditions, and then exhumed, all within ~16 m.y. During exhumation, penetrative deformation by solution mass transfer (SMT) resulted in a widespread spaced cleavage. Strain directions were determined for 27 sandstone samples, and absolute strain measurements for a subset of 19 samples. Z directions generally plunge moderately to the NE, and X and Y directions are scattered in the plane perpendicular to Z. SMT deformation is constrictional at the local scale, but the tensor average indicates plane-strain uniaxial shortening at the regional scale, with S_x, S_y, and S_z equaling 1.01, 0.91, and 0.58, respectively. The average flattening plane (XY) dips 30° to the NE, and the average X direction plunges 20° to the north. The large shortening in Z was compensated by a mass-loss volume strain of ~47%. We present a simple one-dimensional model that illustrates the relationship between finite strain and ductile exhumation for a steady state convergent wedge. Assuming depth-dependent ductile flow and no reversal of principal strain rates with depth, this model indicates that ductile thinning of the SJC nappes accomplished only 13% of the total exhumation, despite a vertical shortening strain of 36%. There is no evidence that normal faulting contributed significantly to exhumation. We conclude that erosion operating at an average rate of ~1.1 km m.y.$^{-1}$ was the dominant exhumation process.

1. Introduction

The occurrence of regionally coherent low-temperature (LT), high-pressure (HP) metamorphic terranes in convergent orogens remains an important tectonic problem. Much attention has been given to understanding the exhumation of these once deeply buried rocks. Three processes are commonly invoked (Figure 1): (1) erosion [e.g., *England,* 1981; *Brandon et al.,* 1998], (2) normal faulting near the top of the wedge [e.g., *Platt,* 1986; *Jayko et al.,* 1987], or (3) ductile flow deeper within the wedge [*Selverstone,* 1985; *Wallis,* 1992, 1995; *Platt,* 1993; *Dewey et al.,* 1993]. Ductile thinning has not received as much attention, but several examples suggest that it might be important. *Selverstone* [1985] proposed that ductile thinning in the eastern Alps was responsible for ~20 km of exhumation recorded by HP metamorphic rocks exposed in the Tauern window. *Wallis* [1992, 1995] used deformation measurements to estimate ~20 km ductile thinning for metamorphic rocks exhumed during Late Cretaceous and early Cenozoic subduction along the SW Japan convergent margin. *Dewey et al.* [1993] argued that vertical ductile shortening, with values up to 80%, was an important factor in unroofing high-pressure (20-28 kbar) metamorphic rocks in the SW Norwegian Caledonides.

In this paper, we focus on the hypothesis of *Platt* [1986] that underplating beneath a thick accretionary wedge, coupled with viscous ductile flow within the wedge, might lead to vertical thinning within the upper part of the wedge, either in the form of normal faulting or in the form of ductile flow (Figure 1). *Pavlis and Bruhn* [1983] and Platt argued that a Coulomb rheology might not be appropriate for wedges thicker than ~15 km because thermally activated ductile deformation mechanisms should start to control the strength of the wedge. In convergent wedges dominated by LT-HP metamorphism, the dominant ductile deformation mechanism is pressure solution or solution mass transfer (SMT). This mechanism gives rise to a distinctive semi-penetrative cleavage, which is generally best developed in sandstones and mudstones. Temperatures in a LT-HP setting are commonly too low for intragranular deformation mechanisms, such as dislocation glide, to contribute significantly to the overall deformation. There is growing empirical evidence that SMT is the dominant ductile deformation mechanism in LT-HP wedges to depths and temperatures up to 35 km and 300°C [*Norris and Bishop,* 1990; *Fisher and Byrne,* 1992; *Brandon and Kang,* 1995; *Schwartz and Stöckhert,* 1996; *Ring and Brandon,* 1999].

The wedge model considered by *Platt* [1986] has a mixed flow field (Figure 2a), involving vertical thickening at depth and vertical thinning near the surface. This case is only one of three end-members for flow in a wedge (Figure 2). The term flow is used here in a general sense to indicate the motion of material through the wedge, as is illustrated by the schematic flow lines in Figure 2. The flow lines provide some information about the velocity-gradient field within the wedge: convergence or divergence between the lines indicates shortening or extension in that direction. The deformation is assumed to

Paper number 1998JB900054.
0148-0227/99/1998JB900054$09.00

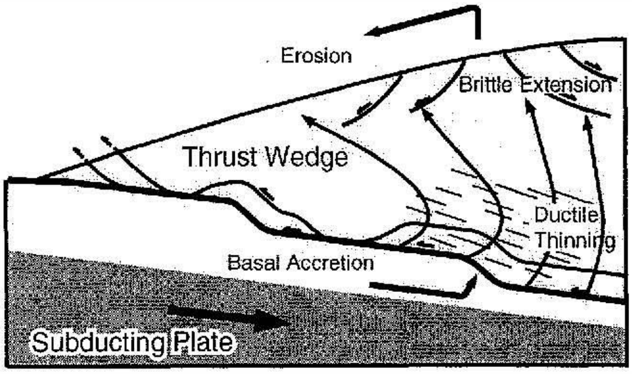

Figure 1. Schematic illustration of material flow through a convergent wedge. Exhumation at the back of the wedge occurs through a combination of ductile thinning, brittle faulting, and erosion.

be continuous at the scale of the entire wedge, but it may involve both continuous and discontinuous processes at the local scale, such as penetrative ductile flow or slip on spaced faults. The mixed flow case (Figure 2a) was first indicated by the analogue modeling experiments of *Cowan and Silling* [1978]. *Platt* [1986, 1987, 1993] developed the idea more fully and outlined a number of convergent wedges where mixed flow might have occurred. The diagnostic feature of a mixed flow wedge is that material moving through the wedge experiences a reversal in the principal strain-rate directions.

Other kinds of flow fields are possible. A thinning flow field (Figure 2b) would be characterized by contractional vertical strain rates everywhere along the exhumation path. Measurements of ductile SMT deformation in the Eastern Belt of the Franciscan Complex of California indicate that the Franciscan wedge probably had a thinning flow field [*Ring and Brandon*, 1999]. A thickening flow field (Figure 2c) would be characterized by extensional vertical strain rates everywhere along its exhumation path. The Cascadia accretionary wedge of western Washington State probably has a thickening flow field as is indicated by vertically lineated rocks observed where the wedge has been uplifted and deeply exhumed in the Olympic Mountains of western Washington State [*Tabor and Cady*, 1978; *Brandon and Kang*, 1995; *Brandon et al.*, 1998].

Our goal is to use finite-strain measurements from exhumed samples to deduce the flow field that existed within the wedge. Our approach is based on the fact that the strain observed in exhumed rocks accumulated while those rocks moved through the wedge. The Late Cretaceous San Juan-Cascade (SJC) thrust belt is an ideal place for this kind of study because its deformation, metamorphic, and exhumation history is well understood [*Brandon et al.*, 1988; *Cowan and Brandon*, 1994]. Furthermore, syntectonic LT-HP metamorphism indicates that temperatures remained relatively low (< 200° C) throughout the development of the wedge. We first review the regional setting and tectonic history of the SJC nappes. Next, we report the results of our textural observations and strain measurements for sandstones deformed by SMT. We finish with a simple one-dimensional analysis of the contribution that ductile strain has made to exhumation of the SJC wedge.

2. Tectonic Setting

The SJC nappes lie within a top-to-the-SW thrust belt that flanks the SW side of the Coast Mountain orogen. This 230 km-wide orogen formed by Late Cretaceous collision of the Insular superterrane with the western margin of North America [*Brandon et al.*, 1988; *McGroder*, 1991; *Cowan et al.*, 1997]. The SJC nappes are exposed in the San Juan Islands and NW Cascade Mountains (Figure 3). They contain a diverse suite of lower Paleozoic through middle Cretaceous terranes, plus several Upper Jurassic-Lower Cretaceous clastic sedimentary units that were deposited on or adjacent to the older terranes [*Brown*, 1987; *Brown et al.*, 1987; *Brandon et al.*, 1988; *Tabor et al.*, 1994]. At present, the terranes and clastic sequences are imbricated along a system of SE and east dipping thrust faults. *Cowan and Brandon* [1994] estimated that the Rosario and Lopez fault zones in the San Juan Islands (Figures 3 and 4) accommodated a combined slip of >60 km in a top-to-the-SW direction. *McGroder's* [1991] orogen-scale balanced cross section indicated a minimum of 580 km convergence across the entire Coast Mountain orogen, relative to the SW-NE shortening direction determined by *Cowan and Brandon* [1994].

The unifying feature of the SJC nappes is that they all experienced, to some degree, a LT-HP metamorphism charac-

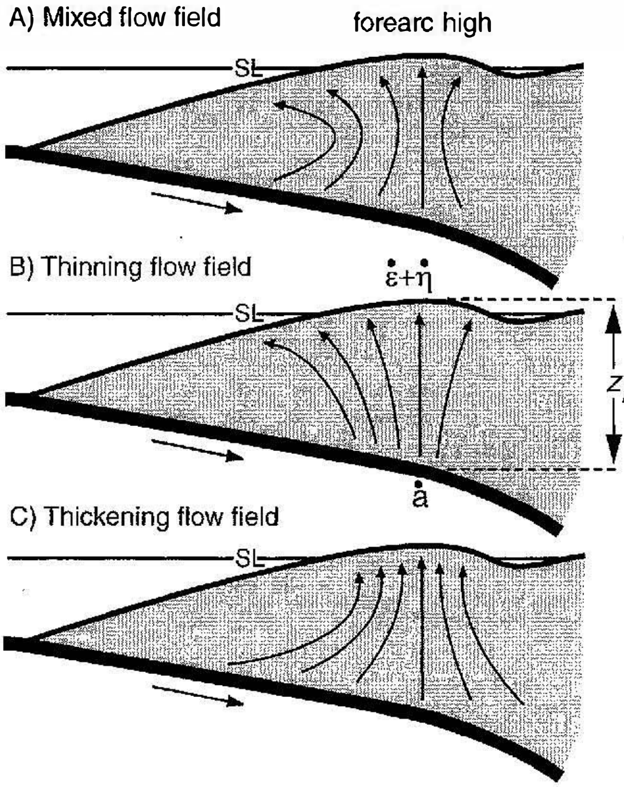

Figure 2. Schematic illustrations of flow fields for three end-member steady state wedges: (a) a mixed flow field, (b) a thinning flow field, and (c) a thickening flow field. Variables shown are: $\dot{a}$ is the rate of basal accretion, z_b is the initial depth of accretion, and $\dot{\varepsilon}+\dot{\eta}$ is the combined exhumation rate for erosion and shallow normal faulting. SL indicates sea level.

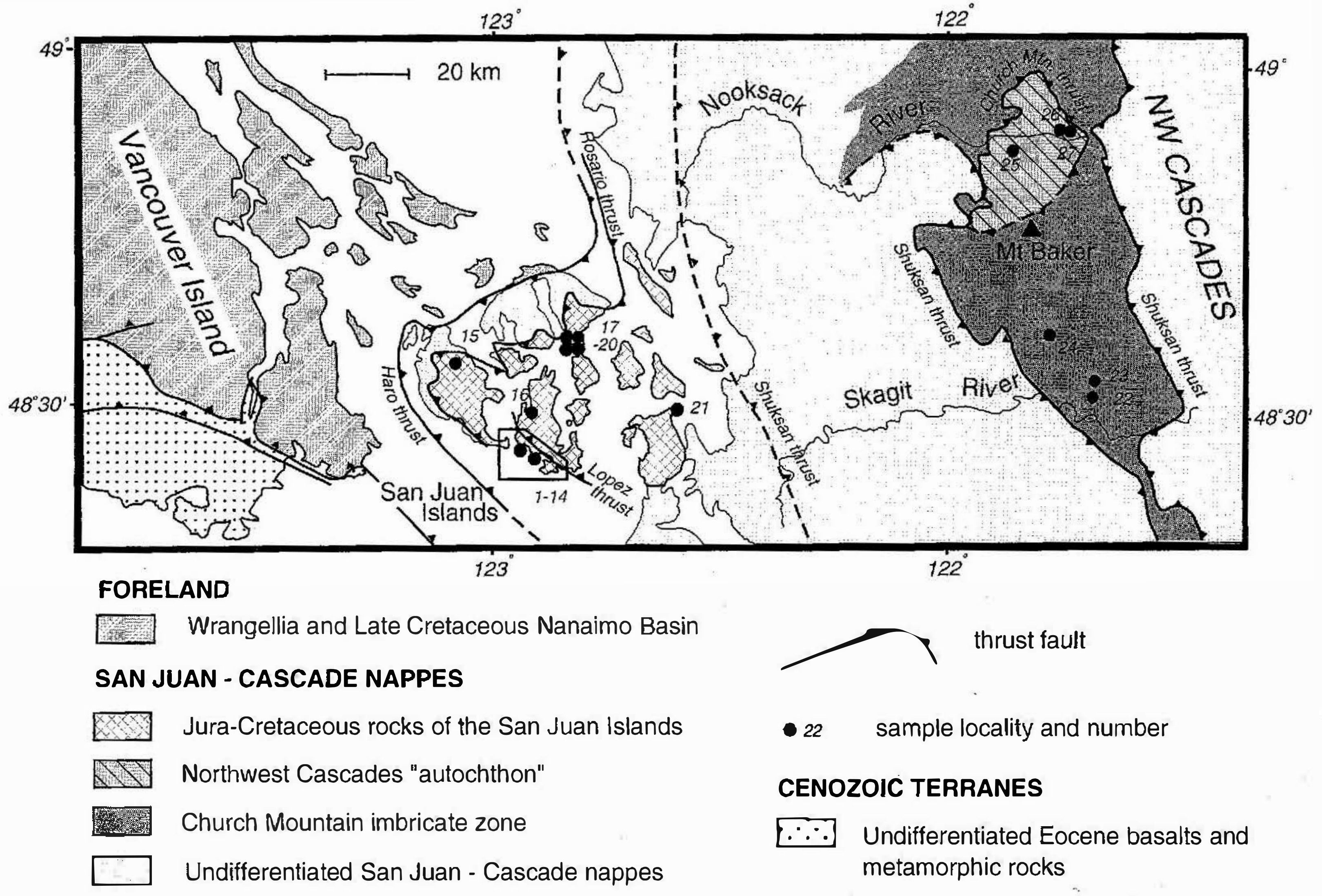

Figure 3. Generalized geologic map of the San Juan Islands and NW Cascade Mountains. Sample locations are shown by dots and numbers. After *Misch* [1977], *Brown et al.* [1987], *Brandon et al.* [1988], *McGroder* [1991], and *Tabor et al.* [1994].

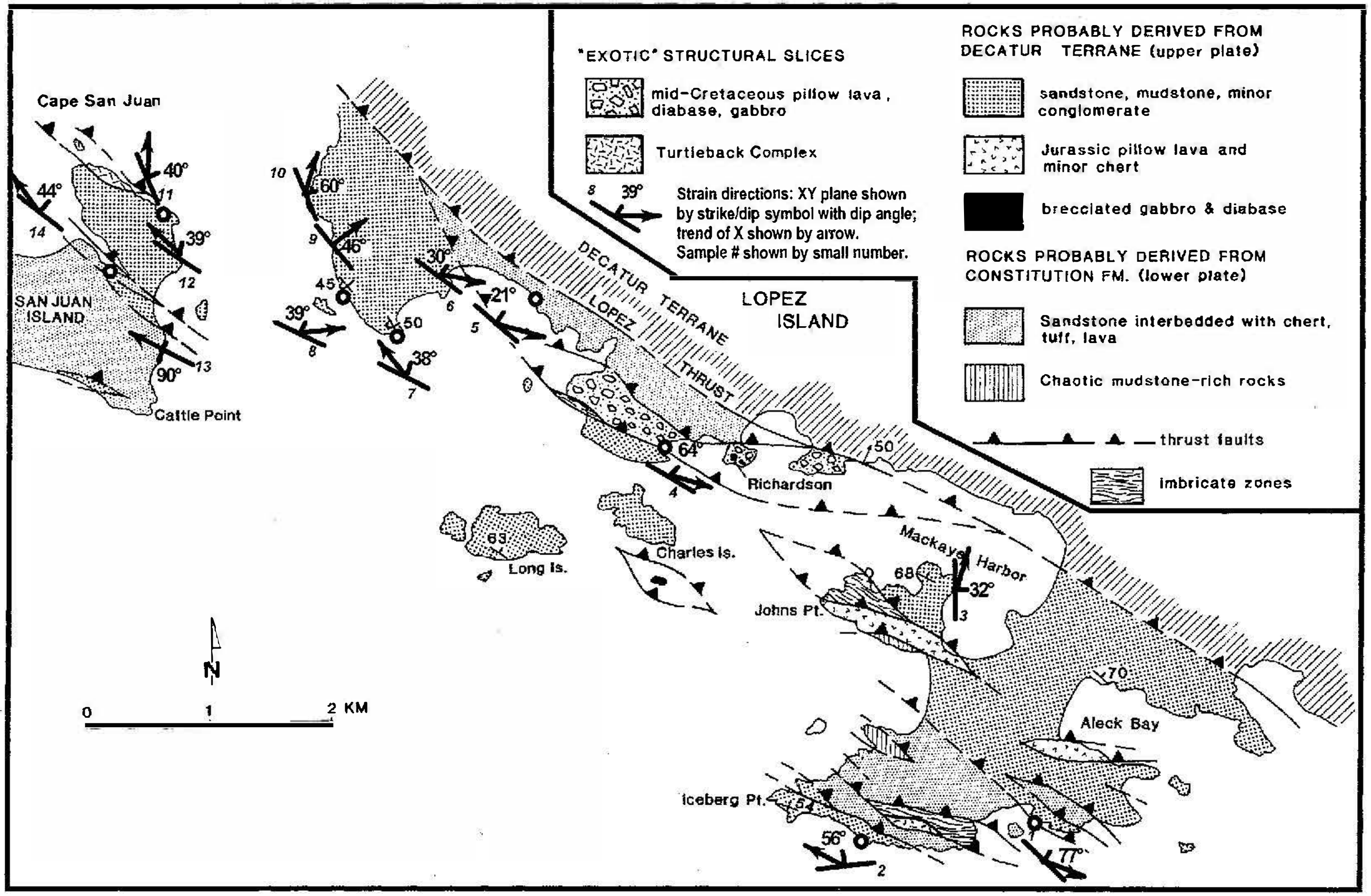

Figure 4. Geologic map of the Lopez Structural Complex, which is exposed on southern Lopez and eastern San Juan Island. The hox in Figure 3 over the San Juan Islands shows the location of this map. The legend shows units within the Lopez Complex. All contacts in the map are faults. The upper limit of the complex is defined by the Lopez thrust and overlying ophiolitic rocks of the Decatur terrane (diagonal ruled pattern). The large foliation-lineation symbol shows the orientation of the strain data reported in Table 1. The foliation attitude is the flattening plane of the strain ellipsoid and the arrow indicates the trend of the maximum extension direction. Sample numbers are indicate by small numbers. The small foliation symbol shows bedding attitudes in stratified units. After *Brandon et al.* [1988].

terized by widespread development of assemblages containing variable amounts of prehnite, high-aluminum pumpellyite, aragonite, and lawsonite [*Vance*, 1968; *Glassley et al.*, 1976; *Brown*, 1987; *Brandon et al.*, 1988]. In the San Juan Islands the Haro thrust juxtaposed the SJC nappes against relatively unmetamorphosed clastic strata of the Upper Cretaceous Nanaimo Group (Figure 3). The Nanaimo Group contains synorogenic conglomerates with clasts of lawsonite+pumpellyite-bearing sandstone, chert, and blueschist derived from the SJC nappes [*Brandon et al.*, 1988]. Thus the Nanaimo basin is thought to represent a foreland basin that was locally overridden by the advancing nappes.

The relative timing of thrust faulting, LT-HP metamorphism, cleavage formation, and exhumation in the San Juan Islands is discussed in *Brandon et al.* [1988] and *Cowan and Brandon* [1994]. The following evidence indicates that slip on the major thrust faults largely predated LT-HP metamorphism:

1. Cataclastic fabrics within the fault zone are overprinted by unfractured and newly crystallized LT-HP metamorphic minerals, present both in veins and as a replacement of detrital grains. Most notable is that this textural relationship is found in highly brecciated exotic fault slices scattered along the Rosario and Lopez fault zones, two of the major fault zones in the San Juan Islands. LT-HP metamorphism must have postdated the emplacement of these slices in the fault zone.

2. A systematic pattern of metamorphic assemblages is observed in the San Juan Islands with higher temperature assemblages found at increasing structural depth. This pattern is taken as evidence that the nappes preserve a coherent structural sequence that was metamorphosed after thrust faulting. In turn, textural evidence indicates that SMT cleavage postdated, at least in part, the peak of LT-HP metamorphism. For instance, *Cowan and Brandon* [1994] showed examples of lawsonite veins that were folded or boudinaged depending on their orientation with respect to cleavage.

Thrusting and metamorphism of the nappes in the San Juan Islands are constrained by the 100 Ma age of the youngest rocks involved in thrusting and by the 84 Ma age of the Nanaimo conglomerates with SJC-derived cobbles [*Brandon et al.*, 1988]. Apatite fission track ages indicate cooling and exhumation of the nappes over this 16-m.y. time interval [*Brandon et al.*, 1988]. The fact that the SJC nappes preserve metamorphic aragonite and Late Cretaceous apatite fission track ages indicates that present exposures have been in the uppermost crust since ~84 Ma (temperature < ~80°C and depths < 3-4 km). Thus we are confident that our measurements of SMT strains are representative of deformation within the SJC wedge and have not been significantly modified by younger events.

Timing is not as tightly constrained in the more eastern SJC nappes, which crop out in the NW Cascade Range. The youngest rocks involved in thrusting there were the Nooksack Group, which includes strata as young as Hauterivian (~135 Ma) and the Easton Metamorphic Suite, which was regionally metamorphosed to blueschist facies during the Early Cretaceous (~120-130 Ma). The Easton makes up the Shuksan plate, which is presently the highest nappe exposed within the SJC nappes; its emplacement postdates its Early Cretaceous metamorphism [*Misch*, 1977; *Brown and Blake*, 1987]. Blueschist cobbles correlative to the Easton are found in Nanaimo Group conglomerates [*Vance*, 1975], indicating exhumation of the Shuksan nappe during the Late Cretaceous. Deposition in the Nanaimo foreland basin ceased at the end of the Cretaceous [*Pacht*, 1984], which implies that thrusting was largely finished by that time. The Eocene Chuckanut Group is the oldest unit that definitively overlies the SJC nappes, both in the NW Cascades and in the eastern San Juan Islands [*Vance*, 1975; *Johnson*, 1984].

Timing relationships and age constraints, especially those preserved in the San Juan Islands [*Brandon et al.*, 1988; *Cowan and Brandon,* 1994], indicate that rocks of the SJC wedge saw the following events between 100 and 84 Ma: (1) rapid subduction and subsequent underplating along a system of brittle faults operating at the base of a convergent wedge, (2) LT-HP metamorphism at maximum pressure-temperature (P-T) conditions soon after accretion, (3) slow development of an SMT cleavage resulting from sustained deviatoric stresses within the wedge, and (4) a return to the surface by exhumation. Given the short time involved, only 16 m.y., it seems likely that some of these events might have overlapped in time. For example, SMT deformation would have been expected to start prior to accretion given that deviatoric stresses probably increased rapidly during subduction of the nappes beneath the wedge. Even so, the textural evidence indicates that brittle faulting predated the development of SMT fabrics.

We envision that subduction and accretion occurred very quickly, leaving little time for SMT deformation to accumulate during subduction. This interpretation is supported by the consideration of subduction rates at typical accretionary wedges. Accretionary wedges have an average surface slope of ~3° and a décollement dip of ~5° [*Davis et al.*, 1983], which implies that ~7.1 km of convergence would have been needed to get 1 km of structural burial. Thus the 18 km of structural burial of the SJC nappes would have required ~125 km of convergence, which would take ~2.5 m.y., assuming a typical subduction zone convergence rate of 50 km m.y.$^{-1}$. From this we infer that the SJC nappes spent only a short period of time moving along the subduction thrust and a much longer interval, perhaps ~14 m.y., in residence within the wedge.

Davis et al. [1983] and *Dahlen and Barr* [1989], among others, have argued that a Coulomb wedge must deform internally in a pervasive and brittle fashion to maintain its taper. We see little evidence for significant brittle deformation in the SJC nappes after their accretion. Map-scale faults appear to entirely predate cleavage and metamorphism as is indicated by the coherent distribution of cleavage and metamorphic assemblages at the regional scale. The major nappe-bounding faults would have been prone to reactivation during younger deformation, but we have already noted evidence that cataclastic fabrics within the fault zones were overprinted by cleavage and LT-HP metamorphic assemblages. Late-stage brittle structures are locally observed at the outcrop scale and in thin section, but they tend to have wide spacing and small offsets, which suggests that their contribution to within-wedge deformation was negligible. On the basis of this evidence, we infer that the taper of the SJC wedge was maintained by distributed underplating and within-wedge ductile flow, and not by brittle faulting. *Ring and Brandon* [1999] came to a similar conclusion in their study of SMT deformation in the Franciscan accretionary wedge.

3. Sampling

In the field the most obvious expression of SMT deformation is a semipenetrative anastomosing cleavage, which is best developed in sandstones and mudstones. In the San Juan Islands the cleavage generally dips NE at a gentle to moderate angle [*Brandon et al.*, 1988; *Cowan and Brandon*, 1994]. The cleavage orientation has not been systematically studied in the NW Cascades, but our reconnaissance indicates similar orientations there.

Sampling was restricted to medium-grain sandstones from the Upper Jurassic-Lower Cretaceous clastic units (see Figures 3 and 4 for sample localities). Our strategy was to avoid those terranes that were metamorphosed and deformed before accretion (e.g., the Permian-Triassic Garrison and Vedder schists, the Early Cretaceous Easton schist, and the early Paleozoic Turtleback and Yellow Aster igneous complexes [*Brandon et al.*, 1988]). By sampling the Jurassic-Cretaceous clastic units we ensure that our measurements are representative of deformation that occurred within the SJC wedge. We focused on sandstones because SMT textures are well displayed in these rocks and because detrital grains can be used as strain markers.

Most samples come from the Lopez Structural Complex, exposed in the southern part of the San Juan Islands. Other sampled units include the Constitution and Obstruction formations of the San Juan Islands [*Garver*, 1986; *Brandon et al.*, 1988] and the Nooksack Group of the NW Cascades [*Brown et al.*, 1987]. The Nooksack samples were collected from stratigraphically coherent units that form the structurally lowest part of the Mount Baker thrust window ("Autochthon" of *Misch* [1977]) and from a structurally higher imbricate zone (Church Mount plate of *Misch* [1977]). These units are separated by the Church Mountain thrust (Figure 3). In three cases, our samples are from outcrops that *Brown et al.* [1987] assigned to the upper Paleozoic Chilliwack Group. However, attribution of these outcrops is uncertain. *Tabor et al.* [1994] assigned one outcrop to the Nooksack Group. We favor a Nooksack assignment for all of the outcrops because our samples from there appear similar in all respects to definitive Nooksack sandstones.

4. Microtextures and Deformation Mechanisms

Microtextural observations and strain measurements were made using thin sections cut parallel to the major fabric directions in each rock (Figure 5). Principal strain directions are indicated by X, Y, and Z, corresponding to the maximum, intermediate, and minimum stretches, $S_x \geq S_y \geq S_z$, where stretch S equals the final length divided by the initial length. The XY sections were cut parallel to cleavage, which is assumed to be the flattening plane for SMT strain. Those sections were used to find X, as defined by directed overgrowths on the detrital grains. Then, XZ sections were cut parallel to X and perpendicular to the cleavage plane.

Intragranular fracture and cataclastic textures are commonly observed in the thrust zones that bound the nappes, indicating that most rocks were lithified prior to the time of subduction and accretion. Thus we conclude that intragranular flow was not a significant deformation mechanism after accretion. The fact that sedimentary fabrics are well preserved in SJC sandstones supports this conclusion. The only exceptions are some mudstones that show evidence of local flowage and injection within the larger fault zones [*Cowan and Brandon*, 1994]. Outside of those fault zones, intragranular fractures are rare, which indicates that cataclastic flow did not contribute significantly to within-wedge deformation [*Cowan and Brandon*, 1994].

The most obvious fabric in these rocks is that produced by SMT deformation. Evidence for SMT (Figure 5) includes pressure shadows adjacent to detrital grains, directed fibrous overgrowths inside the pressure shadows, truncated grains, and selvages of insoluble material [cf. *Williams*, 1972; *Mitra*, 1976; *Ramsay and Huber*, 1983].

Some grain-boundary slip must have accompanied SMT deformation to allow for differential extension between grains on adjacent sides of selvage surfaces, but we emphasize that this slip was parallel to the selvages as is indicated by straight fiber overgrowths that are, on average, parallel to the selvages. Furthermore, selvage-parallel slip must have been very small because the selvages are anastomosing and discontinuous in form and generally no more than several grain dimensions in length. If there was open porosity or slip on surfaces oblique to the selvages, as might be expected during general grain-boundary sliding, we would expect to see kinked and curved fibers, which we have not observed. In fact, the observation that almost all of the newly crystallized minerals in the sandstones formed as directed overgrowths indicates that there was little or no porosity during SMT deformation. This conclusion is based on the fact that directed fiber overgrowths are thought to only form where the void space (i.e., crack apertures) is less than several microns across [*Urai et al.*, 1991; *Fisher and Brantley*, 1992]. We note that the SJC sandstones are generally poorly sorted, so mechanical compaction could have removed much of the primary porosity before the onset of SMT deformation.

There is no evidence that other thermally activated mechanisms, such as dislocation glide, contributed significantly to deformation within the wedge. Most quartz and feldspar grains and many of the lithic grains in our sandstone samples are first-cycle volcanic detritus. Quartz generally occurs as monocrystalline grains, showing little or no undulose extinction under polarized light. Some polycrystalline quartz grains do show undulose extinction, but the sandstones also contain minor amounts of metamorphic detritus. The minor fraction of undulose quartz grains could have come from a metamorphic source as well.

Some previous workers have suggested that the cleavage in the San Juan Islands formed as a shear-zone fabric associated with displacement on major terrane boundaries [*Whetten*, 1975; *Maekawa and Brown*, 1991]. This possibility is supported by the casual observation that cleavage intensity appears to be stronger near some fault zones, with the Lopez thrust (Figure 4) providing the best example. There are other areas, however, such as the southern part of Lummi Island, where cleavage is strong but no major thrust fault is nearby. If deformation during cleavage formation was highly noncoaxial, as is predicted by the shear-zone interpretation, we would expect curved or discordant fibers, which are not observed. The fact that the fibers, which record the incremental strain history of the rock, are straight and parallel to the selvages, which closely approximate the finite flattening plane, demonstrates that SMT strain was not due to simple shear but instead accumulated in a coaxial fashion.

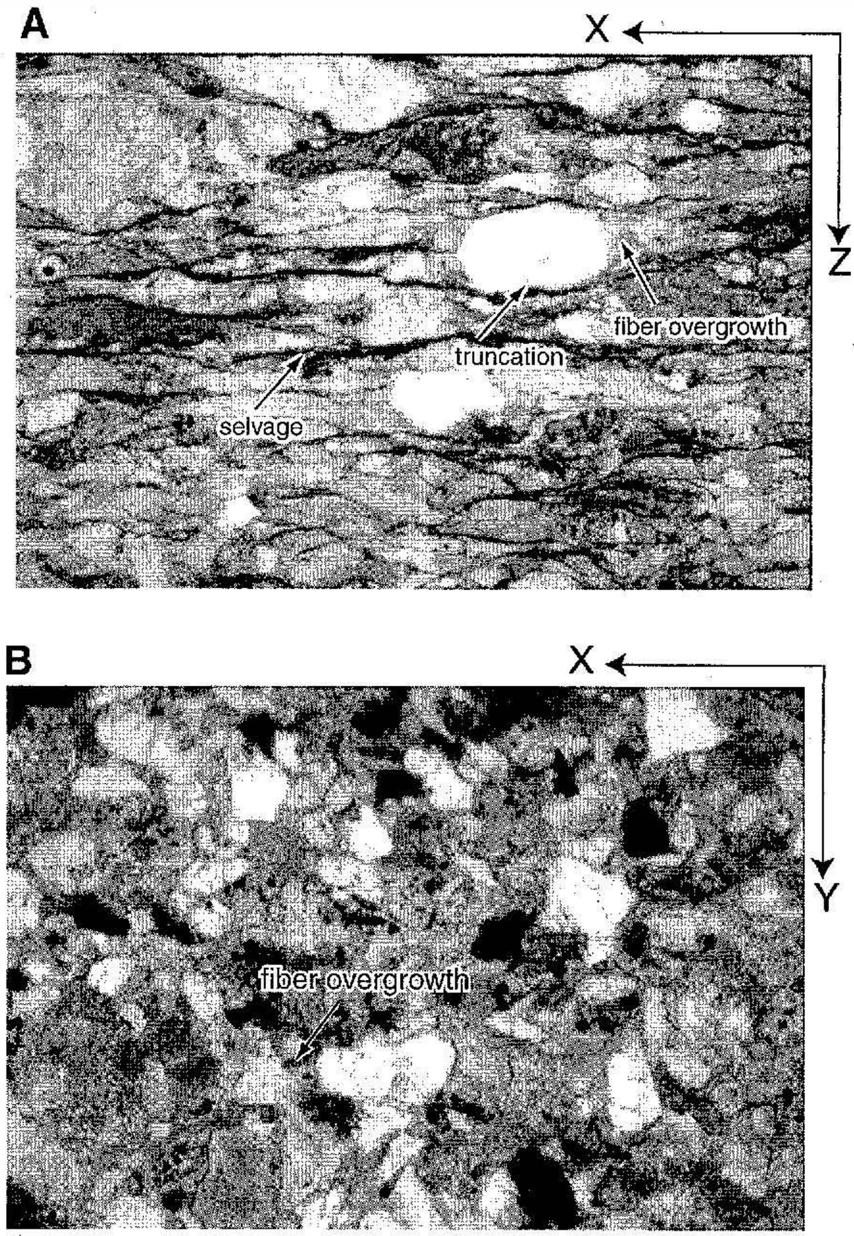

Figure 5. Photomicrographs in plane light showing SMT textures in (a) XZ and (b) XY thin sections for a sample from southern Lopez Island. Images have a long dimension of 2 mm. Dark wispy lines in the XZ section are selvages of insoluble material. Fibrous overgrowths of chlorite, quartz, and white mica are present in pressure shadows around the detrital grains. Note the truncation of the large detrital grains normal to Z in the XZ section. Fibers are nearly everywhere straight and parallel to cleavage, indicating that strain accumulated coaxially. In the XY section, detrital grains are more equant, and pressure shadows are less obvious. Selvages are generally not visible in XY sections.

5. Principal Strain Directions

Principal directions for SMT strain were determined for 27 samples (Figure 6) on the basis of measurements of SMT fabric elements in the XY and XZ thin sections. Uncertainties in determining these directions relative to the present coordinates are estimated to be ~5°-10°. Cleavage commonly has a consistent orientation at local scales (< 5 km). This observation is supported by stereograms in *Cowan and Brandon* [1994] and the strain directions and cleavage orientations shown in map view for the Lopez Complex (Figure 4). When all of the directions are plotted on stereograms in geographic coordinates, Z directions define a steeply dipping, NE striking girdle (Figure 6). Field observations indicate that Z varies at the regional scale (>5-10 km), whereas X and Y are highly variable at both outcrop and regional scales (see Figure 4 for examples).

This variability in principal directions is the result of two independent processes. The first operated at the local scale to produce seemingly random local variations in X and Y. The second was related to minor postorogenic deformation, probably Eocene in age, which produced systematic variations

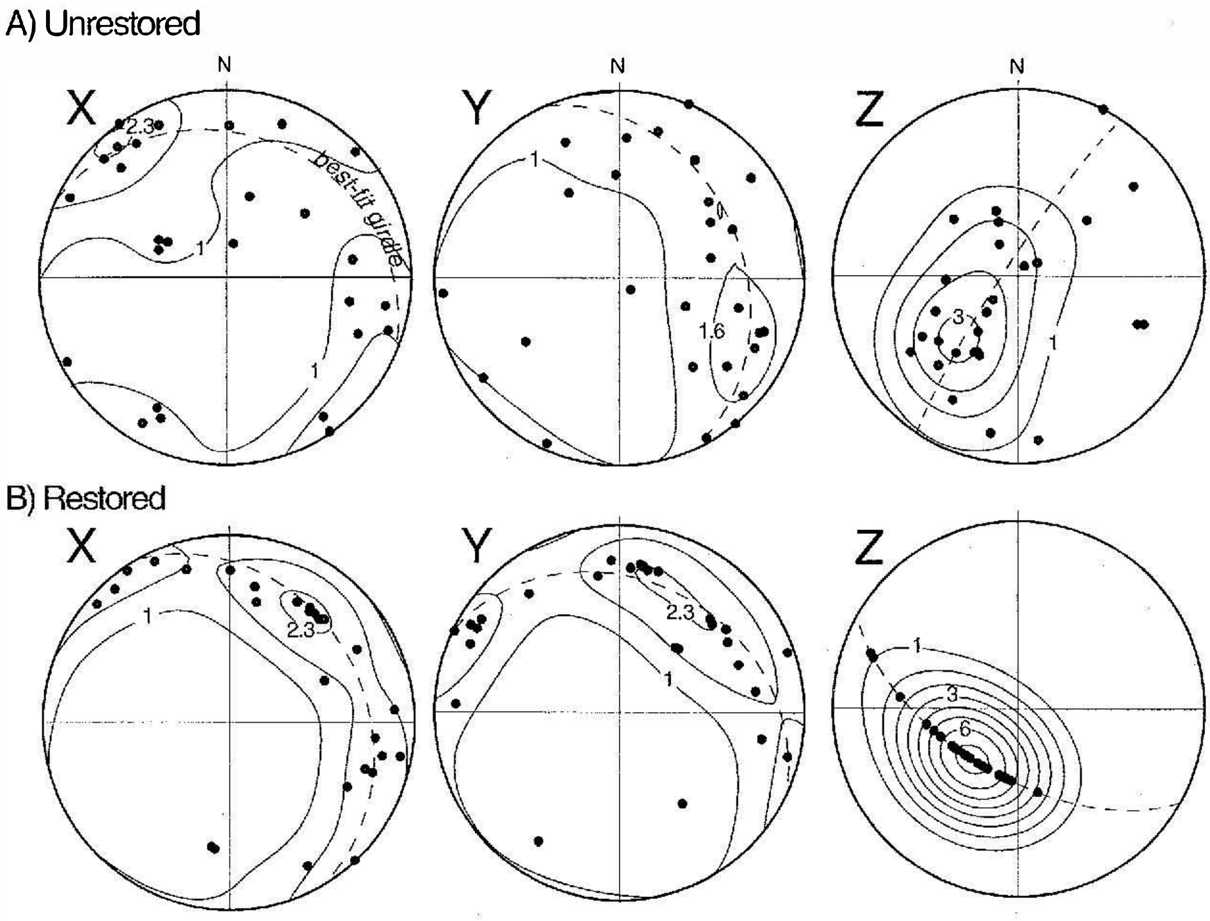

Figure 6. Equal-area stereograms of principal strain directions from the 27 SJC samples used in this study. X, Y, and Z indicate the principal extension, intermediate, and shortening directions, respectively. (a) Unrestored stereograms show principal directions in their present orientations. (b) Restored stereograms show directions after correction for Eocene folding (see text for details). Density contours start at 1 times uniform density and increase in increments of 0.66 times uniform. Areas with densities greater than 2 times uniform are considered to be significantly overpopulated.

at the regional scale. The Eocene deformation is characterized by broad folds that plunge gently to the NW and SE and have ~10 to 15 km wavelengths in the San Juan Islands. These folds are readily apparent in the Upper Cretaceous Nanaimo Group to the north of the San Juan Islands [*England and Calon*, 1991] and in the Eocene Chuckanut Group in the eastern San Juan Islands and the NW Cascades [*Johnson*, 1984]. The thrust faults in the San Juan Islands are folded in a similar fashion around a gently SE plunging axis (Figure 3). The anticlinal form of the Mount Baker thrust window in the NW Cascades may be another manifestation of this deformation. We interpret the girdle in Z directions (Figure 6) to have been produced by this folding event. In the San Juan Islands the horizontal shortening caused by Eocene folding is fairly minor, probably less than 5-10%. Furthermore, the preservation of Late Cretaceous apatite fission track ages in San Juan Islands (discussed above) indicates that this event did not produce much uplift and associated erosion. From this we conclude that Eocene folding occurred at low temperatures and shallow depths. Deformation was probably accommodated by the rigid rotation of fold limbs with local flexural slip on favorably oriented faults and bedding planes.

In order to focus on the Late Cretaceous deformation, we have attempted to remove the effects of the Eocene folding by rotating our measured principal strain directions around an average fold axis defined by the pole to the girdle of Z directions (Figure 6). Each sample was then rotated to bring its Z direction into the plane defined by the average Z direction and the average fold axis. The restored cleavage planes dip, on average, ~30° to the NE. The restored X and Y directions both define girdles that lie subparallel to the average cleavage plane. Even after restoration, X and Y remain highly scattered within the girdle distribution. The density contours show a weak tendency for both X and Y to be oriented down dip, but this observation makes no account for strain magnitudes or the orthogonality that must exist between the principal strain directions.

The fact that the X and Y directions remain scattered even after restoration suggests that this feature is intrinsic to SMT deformation in this area. This conclusion is supported by the observation that the variability of X and Y extends to the local scale. Figure 4 shows several examples where the X and Y strain directions vary considerably between adjacent sample locations. For this reason, we emphasize the tensor average

[*Brandon*, 1995; *Ring and Brandon*, 1999] for our strain data when discussing deformation at the regional scale.

6. Methods for Strain Measurements

Finite strains were determined for 19 samples using the projected dimension strain (PDS) and Mode methods. (All programs used in this study are available at http://hess.geology.yale.edu/~brandon.) These methods, which were developed for this study, provide estimates of absolute stretches and thus permit calculation of volume strains associated with SMT deformation. The PDS method is based on the observation that SMT deformation is controlled entirely by processes operating at the grain boundaries. In directions of shortening, grains converge by dissolution along the grain boundaries. In directions of extension, grains diverge, forming intergranular spaces, which are filled with directed fiber overgrowths. If SMT was the sole ductile mechanism (i.e., no intragranular strain) and if $S_x \geq 1$, then the original dimension of each detrital grain should be preserved in the X direction because the grain surface there is mantled by fiber overgrowth. Conversely, shortening in the rock must have been accommodated by a reduction of the original dimensions of each detrital grain. All samples here have unidirectional fiber overgrowths, which means that they were shortening in both Y and Z (cf. *Ring and Brandon* [1999] who described multidirectional fibers, indicating extension in both X and Y).

The PDS method provides a way of measuring SMT strain in those principal directions where $S \leq 1$. The underlying concept is that the average maximum projected dimension measured in a specified direction for a group of grains in a sandstone must be reduced by a proportion equal to the stretch in that direction. The maximum projected dimension is more commonly called the caliper dimension and can be viewed as the size determined by placing a three-dimensional grain in a caliper with the caliper face oriented in the direction of interest. Stretch is determined by measuring the average caliper dimension for a group of detrital grains in a principal shortening direction (Y or Z in our case) and dividing that value by the average caliper dimension of the same set of grains in the X direction. Because the grain dimensions are conserved in the X direction, the average caliper dimension for the X direction should provide an unbiased estimate of the original average caliper dimension of the grains in the Y and Z directions. This calculation assumes that the initial sedimentary fabric was, on average, isotropic, but it does not require that the individual grains were originally spherical.

To directly measure maximum projected dimensions, it is necessary to have three-dimensional access to each grain. Our measurements were made using two-dimensional thin sections. Only rarely does the section show the maximum dimensions of a grain. As a result, PDS measurements made in a thin section will give a biased stretch, designated as S'. This biased result will tend to be less than the true stretch S. We have found that the relationship of S' to S is well approximated by using a truncated sphere to represent the average three-dimensional shape of a measured set of detrital grains truncated by SMT selvages. The sphere is "shortened" on each side by truncation surfaces oriented perpendicular to the principal shortening direction and symmetric about the center of the sphere. The true stretch S is equal to the ratio of the truncated diameter in the shortening direction over the original diameter of the sphere. The observed apparent stretch S' depends on where the section of view passes through the truncated sphere. Those sections that pass through the center of the truncated sphere will have $S' = S$, whereas those that pass far from the center will tend to show circular sections (i.e., $S' = 1$). The expected average for S' is given by integration of all possible sections passing through the truncated sphere parallel to the shortening direction. The result is

$$\operatorname{avg}(S') = \frac{S\sqrt{1-S^2} + \sin^{-1}(S)}{\pi/2}. \qquad (1)$$

In practice, the PDS method is used with thin section measurements to estimate avg(S') for the section, and then equation (1) is used to solve for the true stretch S. Tests using randomly generated ellipsoids with varying degrees of truncation indicate that equation (1) gives S to within $\pm$ 0.02 as long as the original grain shapes have aspect ratios < 3, which is generally the case for sandstones [*Paterson and Yu*, 1994; *Ring and Brandon*, 1999].

The PDS method has also been tested using shallowly buried sandstones that have not been affected by processes other than deposition, mechanical compaction, and local intragranular fractures [*Ring and Brandon*, 1999; M. T. Brandon and J. G. Feehan, unpublished work, 1995]. The average result is $S_x = S_y = S_z = 1.0$, which is consistent with the absence of SMT fabrics in these sandstones. These tests support our assumption that the caliper dimensions for grains in our sandstones remained, on average, isotropic until the start of SMT deformation. From this, we infer that the PDS method is relatively insensitive to the rigid rotation of grains that accompanies the formation of early fabrics during deposition and mechanical compaction.

The conventional method for measuring extensional stretches in SMT-deformed rocks is to divide the length of the fiber overgrowths on a grain by the section radius of the grain [*Ramsay and Huber*, 1983]. This method tends to overestimate extensional stretches in our samples, perhaps because of a bias toward selecting the most visible fibers, which are usually the longest.

Extensional stretches can be more precisely determined using the mode method, which is based on the modal abundance of fiber overgrowth in the rock. For a rock with unidirectional fibers (i.e., $S_x \geq 1 \geq S_y \geq S_z$), the fiber mode m in an XZ section is related to S_x according to

$$S_x = (1-m)^{-1}. \qquad (2)$$

Fiber modes were determined by the line-integration method using a computer-automated microscope stage that advances at increments of 1-5 μm. Repeat measurements by the same and different operators indicate that standard errors for measured fiber modes are < 5 modal %. Critical requirements for this method are that the detrital grains have not been significantly recrystallized and that the microscopist can make an easy and confident distinction between the three main components of the rock: detrital grains, fiber overgrowth, and selvages. Our rocks meet these requirements. Metamorphic assemblages are present but typically make up < 3% of the rock. Plagioclase is locally replaced by fine fibrous mats of randomly oriented sub-microscopic lawsonite and pumpellyite, but more commonly, the LT-HP metamorphic minerals are found in thin discontinuous veins. In theory, it would be necessary to include the extension caused by veins to fully determine SMT strain, but veins make up, on average, only 1-2% of the rock.

Our measurements provide estimates of volume strain and mass loss resulting from SMT deformation. The PDS measurements give the amount of grain volume removed by dissolution. The mode measurements indicate the amount of that dissolved volume that was precipitated as newly formed fiber overgrowths. The difference indicates a change in volume of the grain mass due to a transfer of mass in or out of the sample. If we consider a representative elementary volume (REV) within the rock defined by a set of material points, then the volume stretch S_v, equal to the ratio of the final volume over the initial volume, describes the net change in volume of the REV during deformation. The principal stretches are related to S_v according to $S_v = S_x S_y S_z$. Volume stretch can result from a transfer of mass in or out of the REV, a porosity change within the REV, or a metamorphic transformation that affect the average density of the mineral grains in the REV [*Brandon*, 1995]. As noted above, the sandstones probably lacked any significant initial porosity at the start of SMT deformation. Furthermore, the PDS method measures changes in grain dimensions and ignores strains due to changes in porosity. We discount changes in grain density because the detrital grains show only minimal amounts of metamorphic transformation. Thus we conclude that our reported volume stretches are a measure of open-system mass transfer at a scale larger than the thin section.

We have estimated the uncertainties associated with our measurements using the bootstrap method of *Efron* [1982]. On average, the stretches have a relative standard error of ~5%. Propagation of these errors indicates that the relative standard error for S_v is ~10%. Some examples of estimated uncertainties for S_v are included in Table 1.

7. Results for Strain Measurements

The strain data are summarized in Table 1 and displayed graphically in Figure 7. The Nadai plot (Figure 7a) indicates that the strain ellipsoids generally have a prolate symmetry. The maximum axial ratio, $R_{xz} = S_x / S_z$, ranges from 1.6 to 2.7. The largest strains are in the Z direction, with S_z ranging from 0.71 to 0.47, indicating a maximum shortening of 29-53%. S_y ranges from 0.94 to 0.65, which indicates that SMT strain is constrictional at the local scale (Figure 7b). Surprisingly, S_x is quite small, ranging from 1.08 to 1.41. Thus the constrictional aspect of the strain is primarily the result of shortening in the Y and Z directions and not extension in X, as is commonly assumed. *Smith* [1988] and *Maekawa and Brown* [1991] argued for much greater extensional strains in these rocks, with S_x ranging from 2 to 6.4. However, their estimates were calculated from relative strain data (i.e., axial ratios) using the assumption of constant volume; they had no direct information about absolute principal strains.

Our determinations of S_v range from 0.47 to 0.67 (Table 1), which indicates that the sandstones have lost 33-53% of their mass during SMT deformation. At the outcrop scale there is no evidence of a sink for this missing mass. Modal measurements were made at several outcrops using ~5 m line traverses. Veins make up no more than 5% by volume of a typical outcrop, with the average closer to 1-2%. Thus we conclude that SMT deformation was mediated by a large flux of fluid that was able to dissolve the sandstones and to transport the dissolved load over large distances, probably several kilometers or more.

Figure 7c and 7d show that volume strain correlates closely with S_z and the deviatoric component of the strain. This correlation suggests that mass transfer controlled both the deviatoric and volumetric components of the strain. In contrast, *Brandon* [1995] and *Ring and Brandon* [1999] found that deviatoric and volumetric strains were decoupled for SMT deformation in the Franciscan Complex.

Tensor averages are used to represent the effect of SMT deformation at the regional scale. The strain measured at a point can be visualized as a product of an average strain, which corresponds to a homogenous strain at some appropriate regional scale, and a perturbation strain, which represents the local departure from the average strain [*Patterson and Weiss*, 1961; *Cobbold*, 1977]. *Brandon* [1995] showed that if the rotational component of the deformation is minor, then the tensor-average strain can be accurately estimated by calculating the average of each component of the natural-strain tensor or Hencky tensor H_{ij},

$$\mathrm{avg}(H_{ij}) = \frac{1}{n}\sum_{k=1}^{n}\left(H_{ij}\right)_k , \tag{3}$$

where the indices i and j indicate the components of the 3x3 tensor and the subscript k indicates the kth tensor out of a total of n measured strain tensors. H_{ij} has the principal stretch directions as its eigenvectors and the logarithms of the principal stretches as its eigenvalues. The eigenvectors and eigenvalues of avg(H_{ij}) give the principal directions and logarithms of the principal stretches of the average stretch tensor.

Two tensor averages are reported in Table 1. The unrestored average is based on the strain data as determined relative to the present geographic frame, and the restored average is based on strain data corrected for Eocene folding. Note that the restored and unrestored averages are similar.

We focus here on the restored tensor, which indicates principal stretches, S_x, S_y, and S_z of 1.01, 0.91, and 0.58, respectively, and a flattening plane (XY) dipping 30° to the NE. A surprising result is that the stretches in the X and Y directions are both nearly equal to one. This reflects the dispersion of the individual X and Y directions in the flattening plane (Figure 6), so that differences in S_x and S_y are averaged out at the regional scale. Thus SMT strain at the regional scale is characterized by uniaxial shortening, whereas individual determinations indicate that strain at the local scale is heterogeneous and constrictional (S_y < 1.0). The regional-scale deformation is kinematically analogous to sedimentary compaction in a basin where vertical shortening is balanced by volume loss and horizontal strains remain close to zero.

Smith [1988] and *Maekawa and Brown* [1991] argued that the SJC nappes were strongly extended in a NW direction, parallel to the strike of the orogen, and that this extension was due to transpressive shear along the Late Cretaceous North American margin. If the strain measurements are considered with respect to orogenic coordinates (average present strike of the orogen is 136°), we obtain average across-strike, parallel-to-strike, and vertical stretches of 0.79, 0.96, and 0.64, respectively. This indicate an average across-strike horizontal shortening of 21%, which is consistent with other evidence discussed above that indicates SW-NE contraction during the Late Cretaceous orogenic event. The average parallel-to-strike horizontal strain is 4% shortening, which indicates that SMT

Table 1. Strain Data for Selected Clastic Units in the San Juan-Cascade Nappes

Sample Number	S_x Trend	S_x Plunge	S_x Stretch	S_y Trend	S_y Plunge	S_y Stretch	S_z Trend	S_z Plunge	S_z Stretch	S_v* V_f/V_i	S_v* RSE, %	Modes, % Fiber	Modes, % Selvage
Lopez Structural Complex, San Juan Islands													
1	113	24	1.27	358	44	0.80	222	36	0.53	0.54	--	20.6	2.5
2	299	56	1.27	33	26	0.86	190	16	0.52	0.57	--	21.1	1.2
3	20	14	1.24	129	26	0.78	267	58	0.59	0.57	6.5	19.6	2.7
4	101	33	1.20	329	46	0.77	208	26	0.71	0.65	6.6	16.9	0.3
5	108	9	1.41	15	20	0.71	221	69	0.53	0.53	--	29.0	0.6
6	100	14	1.25	3	26	0.65	216	60	0.59	0.47	--	19.7	1.1
7	326	15	1.15	67	34	0.78	208	52	0.65	0.58	--	13.2	1.2
8	82	32	1.30	338	23	0.75	206	51	0.54	0.53	--	22.9	2.0
9	51	45	1.20	141	0	0.73	231	44	0.54	0.47	--	17.1	7.5
10	16	53	1.13	133	9	0.90	235	30	0.47	0.48	--	11.8	2.5
11	1	20	--	104	34	--	247	50	--	--	--	--	--
12	314	10	--	50	37	--	210	51	--	--	--	--	--
13	297	7	1.25	135	83	0.72	27	[illegible]	0.52	0.47	6.6	19.7	1.5
14	320	10	--	59	42	0.69	219	46	--	--	--	--	--
Constitution (15), Lummi (16, 21) and Obstruction (17-20) Formations, San Juan Islands†													
15	145	10	--	53	12	--	227	75	--	--	--	--	--
16	208	22	--	111	20	--	341	60	--	--	--	--	--
17	205	18	1.17	110	18	0.77	340	65	0.62	0.56	5.6	14.4	2.3
18	210	11	1.27	117	19	0.72	329	74	0.50	0.45	7.3	21.0	2.8
19	242	4	1.26	151	3	0.70	31	85	0.51	0.45	--	20.4	5.9
20	46	4	1.19	140	38	0.89	311	52	0.53	0.56	--	15.8	1.0
21	316	20	1.08	113	58	0.94	52	23	0.66	0.67	7.5	7.2	0.7
Nooksack Formation, NW Cascades													
22	146	1	1.32	236	39	0.75	51	51	0.49	0.48	7.5	24.5	1.3
23	325	0	--	234	10	--	55	80	--	--	--	--	--
24	12	75	1.08	265	5	0.81	173	13	0.67	0.58	5.7	7.3	1.5
25	336	12	1.26	78	48	0.79	238	39	0.55	0.55	9.5	19.7	1.5
26	301	60	--	204	4	--	111	29	--	--	--	--	--
27	292	58	--	22	0	--	112	32	--	--	--	--	--
Tensor averages													
Unrestored	110	13	0.95	14	26	0.82	224	60	0.68	0.53	--	17.0	1.6
Restored	353	20	1.01	92	23	0.91	226	60	0.58	0.53	--	17.0	1.6

* $S_v = V_f/V_i$ equals final volume over initial volume. RSE is the relative standard error given as a percentage of the measured S_v.

† Numbers in parentheses refer to sample numbers.

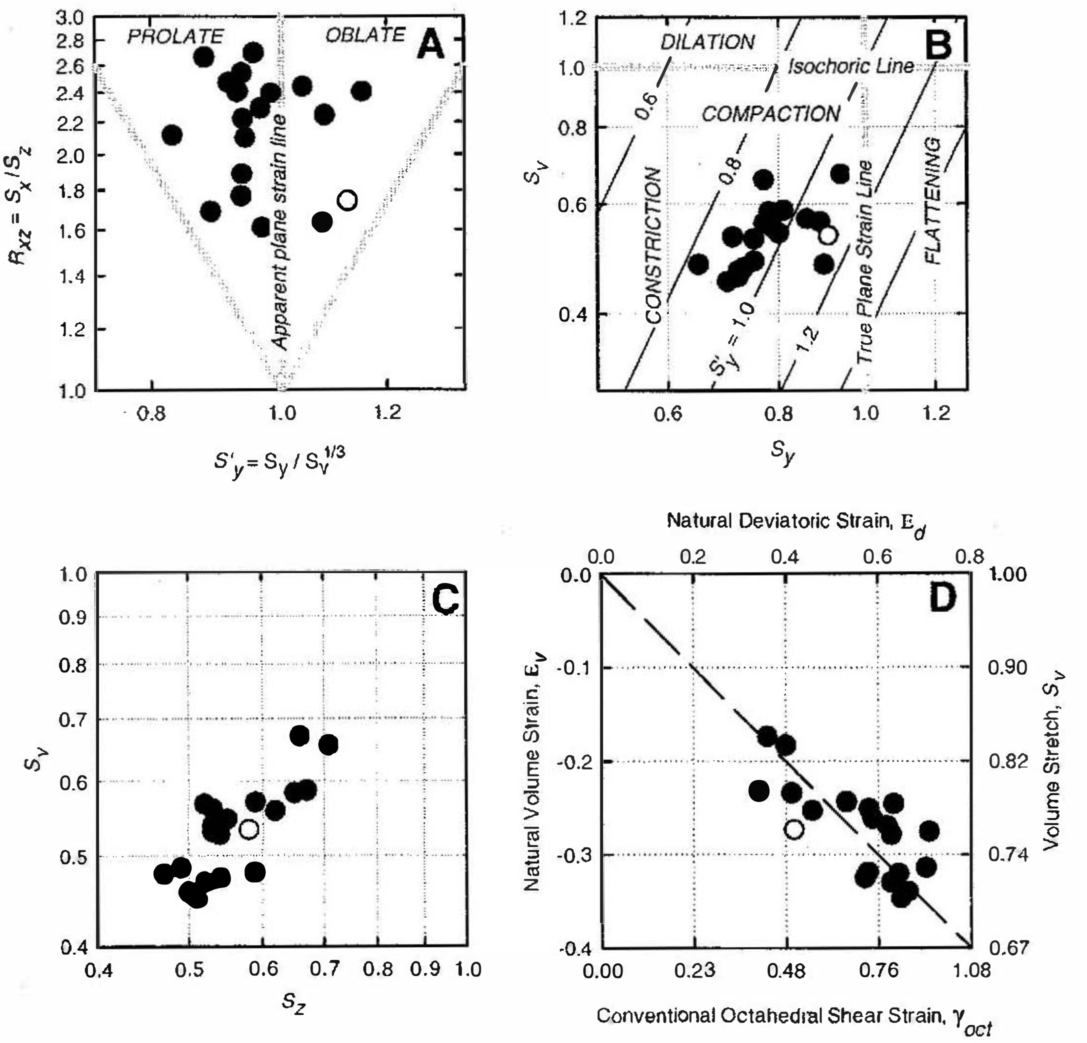

Figure 7. Plots of strain data using methods of *Brandon* [1995]. (a) The Nadai plot indicates the symmetry of the strain, either prolate or oblate. S'_y is the intermediate deviatoric stretch, equal to the S_y normalized to constant volume ($S'_y = S_y - S_v^{1/3}$). Most SJC strain ellipsoids (dots) have prolate symmetry, but the tensor-average ellipsoid (circles) has an oblate symmetry. (b) The strain-type plot, which is based on the absolute magnitudes of the stretches, indicates that the strain is generally constrictional ($S_y < 1$) with a significant compactional volume strain ($S_v < 1$). However, the tensor average (circle) plots near the true plane strain line. Diagonal lines are S'_y contours. (c) The S_v-S_z plot indicates that the volume stretch was mainly accommodated by shortening in the Z direction. (d) The E_v-E_d diagram [*Brandon*, 1995] shows a good correlation, which suggests that volumetric and deviatoric components of the strain were linearly coupled. $E_v = \ln(S_v)$ and is a measure of volume strain. E_d is a measure of the average deviatoric strain, defined by $E_d^2 = (1/3)[(E_x-E_y)^2 + (E_y-E_z)^2 + (E_x-E_z)^2]$, where E_x, E_y, and E_z are the natural logarithms of the principal stretches. For a coaxial deformation, E_v and E_d are linearly related to the principal strain rates. Equivalent values for the volume stretch S_v and the conventional octahedral shear strain E_{oct} are shown on logarithmic axes.

deformation was close to plane strain. Our strain data are at odds with the transpressive shear hypothesis.

8. Models for Ductile Thinning and Exhumation

8.1 Exhumation by Ductile Thinning Alone

Our measurements indicate that SMT deformation caused a vertical shortening of 36% and thus contributed to exhumation of the SJC nappes. To evaluate the tectonic significance of ductile thinning, we first consider a simple model, where exhumation is controlled solely by pervasive ductile deformation of the wedge. In this case, vertical thinning is completely described by the average vertical stretch S_{vert} of the overburden. A particle that started at depth z will move to a new depth $z\,S_{vert}$, with the amount of exhumation given by

$$\delta = z\,(1 - S_{vert}). \qquad (4)$$

S_{vert} would have to be zero (i.e., 100% shortening) for the rocks to become fully exhumed. This example illustrates why ductile thinning alone cannot account for all of the unroofing of a once deeply buried metamorphic rock. Erosion or localized faulting is needed to bring the rocks to the surface.

This simple model is similar in design to that proposed by *Wallis* [1992, 1995] for his analysis of exhumation by ductile thinning. We comment here about his calculation because it may seem at odds with (4) above. Wallis developed an equation for ductile thinning that was based on two parameters: the strain ratio R_{xz} and the mean kinematic vorticity number W_m. Deformation was assumed to be plane and isochoric (constant volume). W_m is defined below, but for now it is sufficient to state that W_m is a measure of the average rate of rotation relative to the average strain rate. The use of W_m implies that the rotational component of the deformation must be specified to calculate the amount of exhumation caused by ductile thinning. In actuality, W_m is not needed if the orientation of the strain ellipsoid is known. Orientation data are usually collected when measuring finite strain, so there is no advantage in using W_m in the calculation. This conclusion is consistent with the fact that S_{vert} is, by definition, the stretch experienced by a material line presently lying in the vertical. Thus one only needs a full determination of the strain tensor to estimate S_{vert} [*Malvern*, 1969, equations 4.5.16 and 4.6.3], assuming, of course, that the strain data are measured relative to the final state, which is always the case in structural geology.

This simple model breaks down when exhumation occurs by more than one process. To illustrate, consider an accretionary wedge in which a material particle is accreted to the base of the wedge and then returned to the surface by a combination of ductile thinning and some shallow process, such as erosion or normal faulting. When shallow exhumation processes are active, the overburden will thin at a faster rate than would occur by ductile thinning alone. As a result, each increment of vertical strain is distributed over a thinner section of overburden, which means a smaller increment of ductile thinning relative to that predicted by the simple model. The ductile thinning rate will also be influenced by any depth dependence in the ductile deformation rate. These examples show that the contribution of ductile thinning to exhumation can no longer be determined solely from S_{vert}. A more comprehensive model is needed.

8.2 One-Dimensional Model for Exhumation of a Steady-State Wedge

To assess the contribution of ductile flow to exhumation, we need to estimate the time-depth history for the particle of interest and the velocity-gradient field near the particle path. One problem is that the overburden that used to overlie our samples is now gone, which means that there is no direct information about how that overburden deformed internally. Furthermore, we can only loosely constrain the full deformation history of our strain samples. Thus we make the assumption that the overburden and exhumed samples experienced the same deformational history. This implies a steady state wedge where the accretion rate, erosion rate, and velocity field within the wedge are constant with time. Given a balance between accretion and erosion, a steady state wedge will neither grow nor shrink with time.

Consider a single material path through an idealized steady state wedge (Figure 8). This path can be viewed as the average trajectory for an underplated rock as it moved through the wedge. A x-z coordinate frame is erected with positive z down and positive x toward the rear of the wedge. Material is accreted to the base of the wedge at an initial depth of z_i, and at a rate $\dot{a}$, and then displaced upward through a combination of basal accretion, within-wedge ductile flow, shallow normal faulting, and surficial erosion.

The vertical velocity of a point at z along the material path is given by

$$w(z) = -\dot{\varepsilon} - \dot{\eta} - \dot{\delta}(z) + u(z)\tan\alpha\,, \tag{5}$$

where $\dot{\varepsilon}$ is the erosion rate, $\dot{\eta}$ is the rate of exhumation due to normal faulting, $\dot{\delta}(z)$ is the rate of change in thickness of the wedge above z due to within-wedge ductile flow, $u(z)$ is the horizontal velocity of the material point at z, and α is the dip of the wedge surface. Steady state means that $\dot{a} = w(z_b)$. Exhumation occurs when $w < 0$, and burial occurs when $w > 0$. Note that by representing the exhumation rate due to normal faulting by a constant $\dot{\eta}$, we have ignored the depth range over which normal faulting might operate. We use this abstraction because we are primarily interested in the contri-

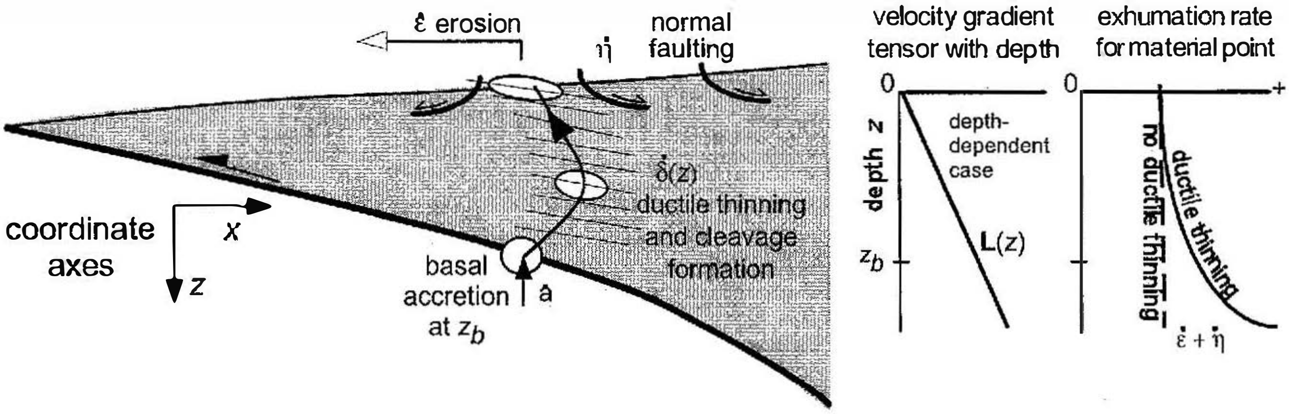

Figure 8. Schematic cross section of a steady state accretionary wedge showing the major processes responsible for vertical thinning or thickening of the wedge and how they affect a particle moving through the wedge along an idealized exhumation path.

bution that within-wedge ductile flow makes to the total exhumation. From here on, we ignore the term $u(z)\tan\alpha$ because real wedges have very gentle surface slopes ($\alpha \approx 3°$) [*Davis et al.*, 1983] and because horizontal velocities u in the back of an underplated wedge should not be significantly greater than the vertical velocities w.

The rate variables $\dot{\varepsilon}$, $\dot{\eta}$, and $\dot{\delta}(z)$ are positive when they contribute to vertical thinning. At steady state, $\dot{\varepsilon}$, $\dot{\eta}$, $\dot{\delta}(z)$, $\dot{a}$, and z_b remain constant with time. In this case, the rate of ductile thinning above z is given by

$$\dot{\delta}(z) = -\int_0^z p_i L(z)_{ij} p_j dz = -\int_0^z L(z)_{33} dz \tag{6}$$

where p_i is a unit vector in the z direction and $L(z)_{ij} = \partial v_i / \partial x_j$ is the velocity-gradient tensor at z, with v_i and x_j referring to the velocity and position vectors at z. Indices follow the standard Einstein summation convention. Note that $L_{ij}=D_{ij}+W_{ij}$, where D_{ij} is the stretching tensor and W_{ij} is the vorticity tensor [*Malvern*, 1969, pp. 146-147]. More specifically, we refer to W_{ij} as the external vorticity [*Means et al.*, 1980] because it is defined relative to the coordinate frame of the wedge. Vorticity can also be represented as a vector with a magnitude of 2ω, where ω is the average rate of rotation of the material around the vector; $\omega > 0$ indicates a right-handed rate of rotation.

Means et al. [1980] and *Lister and Williams* [1983] showed that external vorticity can be accommodated at the local scale through a combination of a rigid-body rotation, called spin, and a shear-induced rotation, called internal vorticity. Note that external vorticity, spin, and internal vorticity are all rates. When integrated along a flow path, they yield finite quantities called external rotation, rigid-body rotation, and internal rotation, respectively. Rock fabrics only provide information about the internal rotation. Our model is not sensitive to this distinction because it is based on external vorticities and external rotations. However, in applying the model, we will need to evaluate how internal rotations determined from rock fabrics relate to the external rotation data needed for the model.

We consider two simple rate equations for SMT deformation: a uniform relationship

$$L(z)_{ij} = \overline{L}_{ij} \tag{7a}$$

and a depth-dependent relationship

$$L(z)_{ij} = \frac{2z\overline{L}_{ij}}{z_b} \tag{7b}$$

In both cases, $\overline{L}_{ij}$ is the depth-averaged velocity-gradient tensor along the entire exhumation path, as is defined by $\overline{L}_{ij} = 1/z_b \int_0^{z_b} L(z)_{ij} dz$. We would prefer to use a rheologically based rate law, but such a law does not exist nor can it be easily specified for a deformation that is strongly mediated by fluid flow and may involve large-scale mass transfer. The uniform relationship in equation (7a) can be viewed as approximating a situation where the rates of dissolution and shortening are governed by a pervasive flow of fluid through the whole wedge. In turn, the depth-dependent relationship (equation (7b)) approximates a situation where the dissolution and shortening rates are governed by parameters that increase with depth, such as deviatoric stress, temperature, and mineral solubility in the fluid phase. Equations (7a) and (7b) are only applicable for steady state wedges with a strictly thinning or thickening flow field (Figures 2b or 2c). A more complicated rate relationship would be needed to model steady state wedges with mixed flow fields (Figure 2a).

Substitution of (7) into (6) and (5) gives

$$w(z) = -\dot{\varepsilon} - \dot{\eta} + z\overline{L}_{33} \text{ and} \tag{8a}$$

$$w(z) = -\dot{\varepsilon} - \dot{\eta} + \frac{z^2\overline{L}_{33}}{z_b}, \tag{8b}$$

where (8a) and (8b) are derived from the uniform and depth-dependent relationships, respectively.

Our objective is to use our measurements of SMT deformation and initial accretion depth to estimate $\dot{\varepsilon}$, $\dot{\eta}$, and $\overline{L}_{ij}$. First, we need to establish the relationship between the instantaneous deformation described by $\overline{L}_{ij}$ and the finite deformation that a material particle acquires while moving along its trajectory through the wedge. Finite deformation at a material point is described by the deformation-gradient tensor $F(t)_{ij} = V(t)_{ik} R(t)_{kj}$, where V_{ik} is the left stretch tensor and R_{kj} is the rotation tensor [*Malvern*, 1969]. Following the same terminology for vorticity, this rotation is an external rotation because it is defined relative to the wedge reference frame. The external rotation can also be described by a vector and a rotation angle Ω, where $\Omega > 0$ indicates a right-handed rotation relative to the vector. The evolution of $F(t)_{ij}$ is given by

$$D_t F(t)_{ij} = L(t)_{ik} F(t)_{kj}, \tag{9}$$

where D_t indicates the derivative of $F(t)_{ij}$ with respect to a reference frame that moves with the material point [*Malvern*, 1969; *McKenzie*, 1979]. Equation (9) contains nine coupled differential equations, one for each of the nine components of $F(t)_{ij}$. Equation (8) provides a tenth differential equation, which tracks the path of the material point through the wedge. Because this additional equation defines the relationship between the differentials of depth and time, dz and dt, we can replace $L(t)_{ik}$ in (9) with $L(z)_{ik}$ as defined by (7). The resulting equations are

$$dF(t)_{ij} = L(z)_{ik} F(t)_{kj} dt \text{ and} \tag{10a}$$

$$dz(t) = [-\dot{\varepsilon} - \dot{\eta} - \dot{\delta}(z)]dt. \tag{10b}$$

This system of differential equations is integrated numerically using the Runge-Kutta method [*Press et al.*, 1990]. Initial conditions at $t = 0$ are set at $z = z_b$ and $F_{kj} = I_{kj}$ (identify matrix) to simulate the accretion of undeformed material to the base of the wedge. The integration is continued until the material point reaches the top of the wedge at $z = 0$ and $t = \tau$.

The integration of (10) describes the forward problem, relating variables $F(t)_{ij}$ and $z(t)$ to the parameters $\dot{\varepsilon}$, $\dot{\eta}$, and $\overline{L}_{ik}$. Our objective is to solve the inverse problem where the parameters $\dot{\varepsilon}$, $\dot{\eta}$, and $\overline{L}_{ik}$ are estimated from our measurements of $F(\tau)_{ij}$ and z_b. Equation (10) does not distinguish between exhumation by erosion or normal faulting, both of which are assumed to operate near the surface of the wedge. Thus we can only solve for the sum $(\dot{\varepsilon}+\dot{\eta})$. The result is an evenly determined inverse, with 10 equations and 10 unknowns. We solved for parameters $(\dot{\varepsilon}+\dot{\eta})$ and $\overline{L}_{ik}$ numerically by using the forward calculation defined by (10), together with an iterative search algorithm, Amoeba, from *Press et al.* [1990].

Given a solution, we can calculate the total exhumation due to both erosion and normal faulting,

$$\varepsilon+\eta=\tau(\dot{\varepsilon}+\dot{\eta}). \tag{11}$$

The absolute contribution of within-wedge ductile deformation to the overall exhumation is

$$\delta=z_b-\tau(\dot{\varepsilon}+\dot{\eta}), \tag{12}$$

and the relative contribution is

$$f_\delta=1-\frac{\tau(\dot{\varepsilon}+\dot{\eta})}{z_b}. \tag{13}$$

9. Application of the Exhumation Model to the SJC Nappes

Two critical assumptions for application of the model are (1) that the flow field within the wedge was either thinning or thickening but not mixed (Figure 2), and (2) that ductile deformation and exhumation occurred while the wedge was at steady state. Deformation textures and strain measurements indicate vertical coaxial thinning during SMT deformation, with no evidence of a reversal in principal strain directions. Thus we infer that the SJC wedge had a thinning flow field.

The steady state assumption is more difficult to assess, but there is good evidence indicating that when the clastic units studied here were accreted, the wedge was probably close to steady state. We used *McGroder's* [1991] orogen-scale balanced cross section to estimate the amount of convergence completed at the time of the accretion of the sampled nappes. Our calculations are summarized in Table 2. The total convergence of the Insular superterrane (Wrangellia of Vancouver Island; see Figure 3) beneath the outboard SW vergent side (SJC wedge) of the Coast Mountain orogen is estimated to be >535 km. Of the clastic units studied here, the first to be accreted were the Lummi and Obstruction formations. By that time, the SJC wedge had already accommodated >170 km of convergence. The last unit of our study to be accreted was the Nooksack Group. At that time, the SJC wedge had accommodated >455 km convergence. Following accretion of the Nooksack, there was an additional >80 km of convergence before the SJC wedge reached its final contracted state.

Synorogenic erosion of the SJC wedge is recorded in foredeeps on both sides of the orogen, the Methow basin to the NE and the Nanaimo basin to the SW [*Brandon et al.*, 1988; *McGroder*, 1991]. *Garver* [1986] showed that the Obstruction Formation in the San Juan Islands was formed in a synorogenic basin adjacent to the SJC nappes. The Obstruction shows the same SMT strains (samples 17-21 in Table 1 and Figure 3) as do other clastic units in the SJC nappes. The conclusion is that SJC wedge was being synorogenically eroded at the time the first units of our study were being accreted. Timing constraints indicate exhumation rates ≥ 1 km m.y.$^{-1}$ (subduction to 18 km, followed by exhumation, all in 16 m.y.). There is little evidence of normal faulting in the SJC nappes, so we infer that erosion was the primary near-surface exhumation process. We have already noted apatite fission

Table 2. Estimated Convergence before Accretion of Clastic Units in the SJC Wedge

Nappe Above Clastic Unit		Clastic Units In SJC Wedge	
Overriding Nappe	Amount of Top-SW Convergence Before Initial Motion of Nappe*	Clastic Unit beneath Overriding Nappe	Amount of Top-SW Convergence at Time of Accretion†
Shuksan nappe (including Easton Schist)	>45 km	Lummi and Obstruction Formations	>170 km
Decatur terrane	>115 km	Lopez Complex and Constitution Formation	>240 km
Church Mountain nappe	>330 km	Nooksack Group of the "Autochthon"	>455 km
		Total convergence Accommodated by the SJC Wedge	>535 km

* Determined from *McGroder's* [1991] cross sections, by measuring the shortening between the leading edge of the overriding nappe and the leading edge of the supra-Nason nappe. The supra-Nason marks the highest nappe in the SJC wedge, which is the outboard SW-vergent part of the Coast Mountain orogen. All distances are with respect to the SW-transport direction determined by *Cowan and Brandon* [1994].

† Added 125 km to estimates in the second column to account for subduction of each clastic unit to a depth of 18 km before accretion beneath its overriding nappe (see section 2 for details on the 125-km estimate).

track cooling ages that indicate that the present exposures of the SJC nappes were exhumed during orogenesis to within several kilometers of the surface of the wedge. These observations implies a close balance between accretion and erosion while the clastic units of our study were being accreted, deformed, and exhumed in the SJC wedge.

The initial conditions and parameters required to obtain a solution for the exhumation model are constrained by the following evidence. Textural analysis indicates that significant SMT strains did not start to form until after accretion of the SJC nappes. Thus we set $F(t = 0)_{ij} = I_{ij}$. Estimates of maximum metamorphic pressure and residence time within the wedge indicate that $z_b \approx 18$ km and $\tau \approx 14$ m.y. (assuming that subduction took ~2 m.y.)

Our measured principal stretches define the eigenvectors and eigenvalues of $V(\tau)_{ij}$ at time τ when the sample reaches the end of its path through the wedge. The restored tensor average (Table 1) is used so that SMT deformation is represented at the regional scale. The observation that fiber overgrowths are both straight and parallel to selvages indicates that SMT deformation was coaxial. In other words, the internal rotation was zero, but, as noted above, the external rotation cannot be directly constrained from this information alone. For now, we assume that the external rotation was zero, which means that $R(\tau)_{kj} = I_{kj}$ and $\Omega(\tau) = 0$.

The results of our model calculation are shown in Figure 9. Using the uniform relationship (equation (7a)), $(\varepsilon + \eta) = 14.6$ km, $\delta = 3.4$ km, and $f_\delta = 19\%$. The depth-dependent relationship (equation (7b)) gives $(\varepsilon + \eta) = 15.6$ km, $\delta = 2.4$ km, and $f_\delta = 13\%$. From the SMT strain measurements we calculate that $S_{vert} = 0.63$. The simple model (equation (4)) predicts a much greater amount of exhumation, $\delta = 6.7$ km, which would be appropriate if ductile thinning had acted alone.

These calculations illustrate that the contribution of ductile thinning to exhumation depends on interactions with other exhumation processes, and it also depends on how ductile deformation is distributed with depth. For these examples, ductile thinning makes the smallest contribution when the deformation rate is depth dependent (equation (7b)). The reason is that as a material point rises toward the surface of the wedge, it moves out of the more rapidly deforming part of the wedge. Thus the thinning rate for the remaining overburden is less than that for the other cases (equations (4) and (7a)). This line of reasoning suggests that a dislocation-controlled rheology, which should be strongly nonlinear with depth, would further reduce the contribution of ductile thinning to exhumation. This conclusion holds for any steady state wedge with a thinning flow field.

The model results also allow us to compare various rates. For instance, the uniform relationship indicates a basal accretion rate $\dot{a} = 1.6$ km m.y.$^{-1}$, a ductile thinning rate for the entire wedge $\dot{\delta}(z_b) = 0.5$ km m.y.$^{-1}$, and a surface exhumation rate $(\dot{\varepsilon} + \dot{\eta}) = 1.0$ km m.y.$^{-1}$ For the depth-dependent relationship, the model indicates slightly faster rates: $\dot{a} = 1.7$ km m.y.$^{-1}$, $\dot{\delta}(z_b) = 0.6$ km m.y.$^{-1}$, and $(\dot{\varepsilon} + \dot{\eta}) = 1.1$ km m.y.$^{-1}$. These rates indicate that whole-wedge ductile thinning operated at a significant rate, equal to approximately one third of the accretion rate.

Using the uniform relationship, the model predicts that SMT deformation had a principal shortening strain rate $\dot{e}_3 = -1.2 \times 10^{-15}$ s^{-1}. For the depth-dependent relationship, $\dot{e}_3$ ranges from -2.7×10^{-15} s^{-1} at the base of the wedge to zero at the top of the wedge. These rates are slow compared to strain rates expected for a plate boundary zone. For example, envision that subduction was accommodated by a thick ductile shear zone at the base of the wedge. The maximum shortening rate within this zone would be equal to $\dot{e}_3 = -v_c/2h$ where v_c is the convergence rate and h is the thickness of the shear zone. For a typical accretionary wedge we would expect that $v_c >$ ~10 km m.y.$^{-1}$ and $h <$ ~10 km, which means that $\dot{e}_3$ should be less than (i.e., faster than) about -1.5×10^{-13} s^{-1}.

This calculation indicates that for the SJC wedge, orogenic convergence was accommodated mainly by slip on the basal thrust, or décollement, so that the wedge itself remained largely decoupled from the subducting plate. In this context, SMT deformation can be viewed as a background deformational process that was active throughout the history of the wedge but accounted for only a small fraction of the total orogenic convergence. The SJC nappes did acquire significant

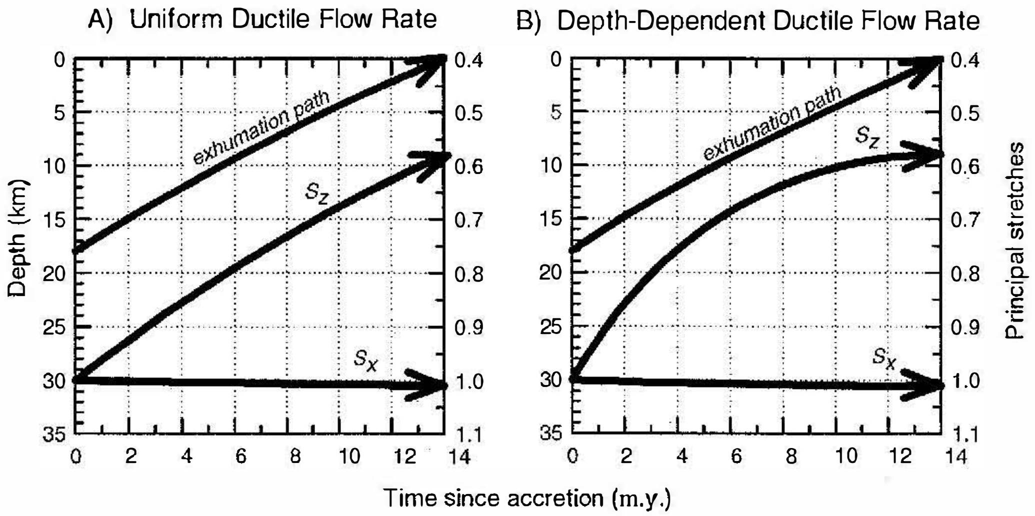

Figure 9. The exhumation model as applied to the SJC nappes, using the restored tensor average (Table 1) to represent within-wedge ductile deformation. See text for details.

deformation by the SMT mechanism. This result reflects the ~14-m.y. period that the nappes spent in the wedge, which allowed a large finite deformation to accumulate from a relatively slow deformation rate.

10. Discussion

The contribution of ductile flow to exhumation in a steady state wedge is determined by the depth dependence of the rate of deformation, the magnitude of the finite strain experienced by the exhumed rocks, and the vorticity of the deformation. We have already examined how ductile thinning is affected by the depth dependence of the ductile flow rate. Here we consider the influence of other factors.

10.1 Influence of Rotational Flow

We assumed in section 9 that the external vorticity was zero during SMT deformation of the SJC nappes. This assumption was based on the observation that SMT deformation was coaxial, meaning that the internal vorticity in the sandstones was zero during deformation. It is possible to have a coaxial rotational flow [*Lister and Williams*, 1983] where the internal vorticity is zero but the external vorticity is not. This can occur when rocks of different competencies are deformed in a shear zone [*Twiss et al.*, 1993] or folded [*Lister and Williams*, 1983]. The external vorticity is partitioned into rigid-body rotation in the competent units and noncoaxial shearing in the incompetent units.

There are two reasons for discounting this explanation for the coaxial fabrics observed in the competent sandstones of the SJC nappes. First, there is no evidence for significant folding during SMT deformation, nor is there any evidence that the nappes are part of a regional-scale ductile shear zone. Second, if vorticity partitioning had occurred, strains and internal rotations would be heterogeneous at the scale of the differentially rotated blocks. We see no evidence for noncoaxial flow in less competent units nor do we find oblique or curved fibers indicating local non-coaxial deformation.

We recognize that it is difficult to prove that ductile deformation was both coaxial and irrotational (i.e., external and internal vorticity both equaling zero). A deformation study of the incompetent units might help to resolve this problem. For now, we consider, in a general way, how a rotational flow might influence ductile thinning.

The kinematic vorticity number W_k of *Truesdell* [1954, p. 107] is a useful parameter for representing the rotational component of a steady deformation. It is defined by

$$W_k = \frac{2\omega}{\sqrt{2}\, D_T}, \qquad (13)$$

where 2ω is the magnitude of the vorticity vector, ω is the average rotation rate around the vector, and D_T is a scalar measure of the average strain rate. More specifically, $D_T^2 = D_1^2 + D_2^2 + D_3^2$, where D_1, D_2, and D_3 are the principal values of the stretching tensor D_{ij} and $\omega^2 = W_{32}{}^2 + W_{13}{}^2 + W_{21}{}^2$, where W_{ij} is the vorticity tensor. When considering a general deformation that might include a volume strain, it is advantageous to replace D_T with a scalar measure of the deviatoric strain rate defined by

$$D_D^2 = (1/3)\left((D_1 - D_2)^2 + (D_2 - D_3)^2 + (D_1 - D_3)^2\right) \quad (14)$$

(see equation 6 in *Brandon* [1995]). D_D describes the average rate of distortion caused by the deformation; it is proportional to the average shear strain rate and independent of the volume strain rate. The modified kinematic vorticity number (distinguished by an asterisk) is

$$W_k^* = \frac{2\omega}{\sqrt{2}\, D_D}. \qquad (15)$$

Irrotational coaxial flow has $W_k = W^*_k = 0$, and isochoric simple shear has $|W_k| = |W^*_k| = 1$. For simple shear with a volume change, $|W^*_k|$ remains equal to one, but $|W_k|$ can take on any value. This illustrates why W^*_k is preferred.

W^*_k is defined using W_{ij} and D_{ij}, so it represents an instantaneous property of the deformation. Nonetheless, W^*_k is dimensionless and therefore independent of the actual deformation rate. In our application here, we consider deformation histories where the components of L_{ij} can change, but only in a proportional way. Thus both the geometry of the deformation and W^*_k will be constant, but the deformation need not be steady.

Figure 10 shows the dependence of f_δ on W^*_k for the range -1 to +1. This calculation assumes a depth-dependent flow rate (equation (7b)) and a vorticity vector oriented parallel to the strike of the orogen (136° trend and 0° plunge). For the anisochoric (nonconstant volume) case, we used the restored tensor average (Table 1). In this case, the variation of W^*_k from -1 to +1 is equivalent to Ω ranging from -22° to +22°. The polarity of the rotation is relative to the vorticity vector, so that a positive W^*_k indicates a top-to-the-SW shear sense and a negative W^*_k indicates a top-to-the-NE shear sense. The conclusion is that for the SJC nappes, the rotational component of the deformation had little influence on the contribution of ductile thinning to exhumation.

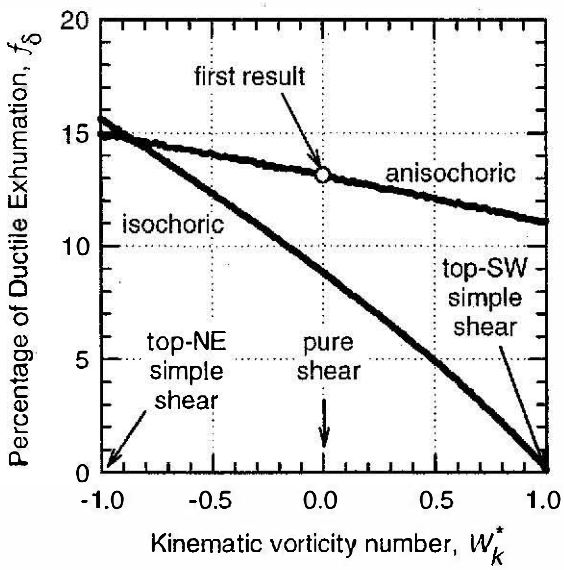

Figure 10. The influence of rotation and volume strain on ductile thinning of the SJC nappes. The "first result" indicates the depth-dependent result calculated in section 9 (also see Figure 9b), where $W^*_k = 0$ and $S_v \neq 1$. The anisochoric curve shows that the rotational component of the deformation has little influence on the contribution of ductile thinning to exhumation. The isochoric curve shows a significant sensitivity to the rotational component of the deformation, but the contribution still remains small, < 16%.

10.2 Influence of Volume Strain

The isochoric case in Figure 10 shows what would happen if volume were conserved during SMT deformation. S_z and Z are the same as used in the anisochoric case above. The deformation is assumed to be plane strain ($S_y = 1$) with the plane of deformation vertical and parallel to the trend of Z. The result is that Y is now defined to lie in the horizontal, parallel to the strike of the orogen. This designation ignores the measured orientation of Y, but it is warranted given that stretches in the XY section are all nearly equal (i.e., $S_x \approx S_y$). In fact, S_z is the only principal stretch of the restored tensor average that is significantly different from one. To mimic an isochoric deformation, we assume that the mass loss observed at the outcrop scale is balanced in some manner by extension at a larger scale, which means that $S_x = 1/S_z = 1.72$. X is assumed to lie in the plane of deformation, indicating a 46° trend and a 30° plunge. The vorticity vector is set parallel to Y.

For this example, the variation of W^*_k from -1 to +1 is equivalent to Ω ranging from -30° to +30°. The greatest ductile thinning occurs when W^*_k = -1, and decreases towards zero as W^*_k increases to +1. These examples show that if the deformation was isochoric, the amount of ductile thinning would generally be less than that predicted for an analogous anisochoric deformation.

10.3 Influence of Strain Magnitude and Strain Orientation

The orientation and magnitude of the principal stretches determine the magnitude of ductile thinning or thickening during exhumation. To examine this problem, we consider an irrotational plane deformation with the Y direction lying horizontal and perpendicular to the plane. The calculation is based on the depth-dependent relationship (equation (7b)). The dip of cleavage (~XY plane) is allowed to vary in 30° increments from 0° to 90°. (Note that the model makes no distinction between a forward or rearward dip.) S_y is set at 1 (i.e., plane strain). S_z is allowed to vary from 1 to 0.1. For the anisochoric case, $S_x = 1$. For the isochoric case, $S_x = 1/S_z$.

Figure 11 shows that very large strains are needed before ductile deformation makes a significant contribution to exhumation. Anisochoric deformation and a gentle dip are factors that enhance ductile thinning. The isochoric examples show that when the cleavage dip is greater than ~45°, ductile deformation will thicken the wedge and thus inhibit the rate of exhumation. This situation does not occur for the anisochoric examples because the deformation is everywhere contractional or zero.

11. Concluding Remarks

Our study demonstrates that SMT was the primary mechanism for deformation within the SJC wedge. The dominance of this ductile mechanism down to depths of 18 km is attributed to the LT-HP conditions in this wedge. What remains odd is the paucity of brittle faulting within the wedge. According to the Coulomb model [*Davis et al.*, 1983], a wedge is only able to slip along its base when it reaches its critical taper. Erosion and frontal accretion will force the wedge into a subcritical taper. It is commonly assumed that the wedge regains its critical taper by deforming internally. One might argue that the Coulomb model is not appropriate for the SJC wedge given the evidence that SMT was the dominant deformation mechanism inside the wedge. However, we have clear evidence that accretion of the nappes occurred by brittle faulting. Thus the base of the wedge had a mixed boundary condition, involving frictionally generated shear stresses and accretionary fluxes, exactly as specified for the Coulomb model.

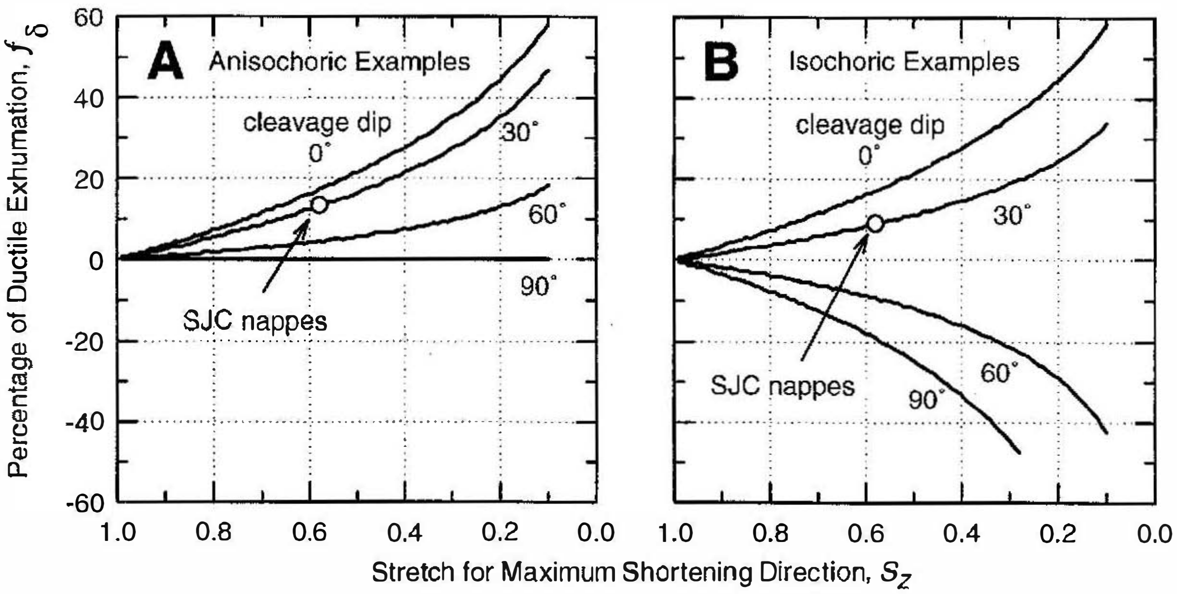

Figure 11. The influence of strain magnitude and strain orientation on ductile thinning. Both plots assume plane deformation ($S_y = 1$), with Y oriented horizontally and perpendicular to the deformation plane. (a) The anisochoric examples assume that $S_x = 1$ and (b) the isochoric examples assume that $S_x = 1/S_z$. The isopleths show the relationship between S_z and f_δ for a specified cleavage dip. The X and Z directions lie in the deformation plane, with the plunge of X equal to the dip of cleavage. The points labeled "SJC nappes" indicate W^*_k = 0 results from Figure 10.

Our exhumation model indicates that ductile flow caused thinning of the SJC wedge at a rate equal to approximately one third of the accretion rate. Thus ductile flow acted together with erosion and frontal accretion to reduce the taper of the wedge. Some other process must have acted to maintain the wedge at a critical taper. A relevant question is how much brittle faulting would be expected if the wedge was maintaining its taper by internal faulting? Judging from *Dahlen and Suppe* [1988], the highest brittle strains should occur when accretion is mainly at the front of the wedge and erosion is mainly at the back of the wedge. The other end-member is an actively accreting wedge with no internal deformation, which occurs when there is uniform accretion along the base of the wedge and uniform erosion at the surface of the wedge.

We propose a model of distributed underplating to explain how the SJC wedge maintained its critical taper with little internal brittle deformation. Erosion, frontal accretion, and slow ductile thinning will cause a Coulomb wedge to become subcritical, but this condition should generally be localized to only part of the wedge at any particular time. The décollement beneath the wedge becomes locked beneath the subcritical segment, but slip remains possible beneath the more rearward segment where the overlying wedge is at critical taper. Localized imbrication and thickening within duplexes along the slipping portion of the décollement would allow the taper to locally increase and the wedge to advance across the locked segment. In this fashion, the wedge could maintain its critical taper by underplating, with little to no deformation within the overlying wedge. This interpretation is consistent with the basic tenet of the Coulomb wedge model, that the critical taper condition is defined by the frictional properties of the décollement and the wedge.

We return to the question raised above: What controls the rates of within-wedge deformation? As shown by *Dahlen and Barr* [1989], the velocity field within a wedge can be fully determined by specifying all of the accretionary and erosional fluxes operating around the boundary of the wedge. In fact, a unique solution is guaranteed, as long as the velocity field is irrotational and isochoric, as assumed by Dahlen and Barr (also see p. 99-104 in *Batchelor* [1967]). It is too early to state if these assumptions are realistic. Our observations of coaxial SMT deformation are consistent with the irrotational assumption, but we do not know if anisochoric flow actually occurs at the scale of the entire wedge. Perhaps volume losses observed in our samples are balanced at some intermediate scale.

The more general point is that different distributions of accretionary and erosional fluxes will give slower or faster rates of internal deformation. Thus the factors controlling the fluxes into and out of the wedge maybe more relevant to understanding deformation within the wedge. For the SJC wedge the distribution of fluxes was apparently appropriate to allow the SMT mechanism to accommodate much, if not all, of the deformation within the wedge. A different distribution of fluxes might have caused higher strain rates and higher deviatoric stresses, perhaps high enough to activate brittle faulting within the wedge.

Acknowledgments. This work was partially supported by Sigma Xi grants to Feehan and a National Science Foundation grant (EAR 9305367) to Brandon. Friday Harbor Marine Lab of the University of Washington provided logistical support in the field. We thank Scott Paterson, Simon Wallis, and Bradley Hacker for constructive reviews.

References

Batchelor, G., *An Introduction to Fluid Dynamics*, Cambridge Univ. Press, New York, 1967.

Brandon, M.T., Representation of geologic strain data in strain-magnitude space, *J. Struct. Geol.*, *17*, 1375-1385, 1995.

Brandon, M.T., and Kang, B., Exhumation processes operating above the Cascadia subduction zone, NW Washington State, *Terra Nova Abst. 7*, 170, 1995.

Brandon, M. T., D. S. Cowan, and J. A. Vance, The Late Cretaceous San Juan thrust system, San Juan Islands, Washington. *Spec. Pap. Geol. Soc. Am. 221*, 81 pp., 1988.

Brandon, M., M. Roden-Tice, and J. Garver, Late Cenozoic exhumation of the Cascadia accretionary wedge in the Olympic Mountains, northwest Washington State, *Geol. Soc. Am. Bull.*, *110*, 985-1009, 1998.

Brown, E. H., Structural geology and accretionary history of the northwest Cascades, Washington and British Columbia, *Geol. Soc. Am. Bull. 99*, 201-241, 1987.

Brown, E. H. and M. C. Blake Jr., Correlation of Early Cretaceous blueschists in Washington, Oregon and northern California, *Tectonics*, *6*, 795-806, 1987.

Brown, E. H, et al., Geologic map of the northwest Cascades, Washington, MC-61, scale 1:100,000, Geol. Soc. Am., Boulder, Colo., 1987.

Cobbold, P. R., Description and origin of banded deformation structures, I, Regional strain, local perturbations and deformation bands, *Can. J. Earth Sci.*, *14*, 1721-1731, 1977.

Cowan, D. S., and M. T. Brandon, A symmetry-based method for kinematic analysis of large-slip brittle fault zones, *Am. J. Sci.*, *294*, p. 257-306, 1994.

Cowan, D. S., and R. M. Silling, A dynamic, scaled model of accretion at trenches and its implications for the tectonic evolution of subduction complexes, *J. Geophys. Res.*, *83*, 5389-5396, 1978.

Cowan, D. S., M. T. Brandon, and J. I. Garver, Geologic tests of hypotheses for large coastwise displacements: A critique illustrated by the Baja British Columbia controversy, *Am. J. Sci.*, *297*, 117-173, 1997.

Dahlen, F., and J. Suppe, Mechanics, growth, and erosion of mountain building, in *Processes in Continental Lithospheric Deformation*, edited by S. Clark Jr., *Spec. Pap. Geol. Soc. Am.*, *218*, 161-178, 1988.

Dahlen, F. A., and T. D. Barr, Brittle frictional mountain building, 1, Deformation and mechanical energy budget, *J. Geophys. Res.*, *94*, 3906-3922, 1989.

Davis, D., J. Suppe, and F. A. Dahlen, Mechanics of fold-and-thrust belts and accretionary wedges, *J. Geophys. Res.*, *88*, 1153-1172, 1983.

Dewey, J., P. Ryan, and T. Andersen, Orogenic uplift and collapse, crustal thickness, fabrics, and metamorphic phase changes: The role of eclogites, in *Magmatic processes and plate tectonics*, *Geol. Soc. Spec. Pub.*, *76*, edited by H. Pritchard et al., 325-343, 1993.

Efron, B., *The Jackknife, Bootstrap, and Other Resampling Methods*, *Conf. Board Math. Sci. - Natl. Sci. Found. Reg. Conf. Ser. Appl. Math.*, vol. 38, Soc. for Ind. and App. Math., 1982.

England, P. C., Metamorphic pressure estimates and sediment volumes for the Alpine Orogeny: an independent control on geobarometers?, *Earth Plane. Sci. Let.*, *56*, 387-397, 1981.

England, T. D. J., and T. J. Calon, The Cowichan fold and thrust system, Vancouver Island, Southwestern British Columbia, *Geol. Soc. Am. Bull.*, *103*, 336-362, 1991.

Fisher, D. M., and S. L. Brantley, Models of quartz overgrowth and vein formation: deformation and episodic fluid flow in an ancient subduction zone: *J. Geophys. Res.*, *97*, 20043-20061, 1992

Fisher, D. M., and T. Byrne, Strain variations in an ancient accretionary complex: Implications for forearc evolution, *Tectonics*, *11*, 330-347, 1992.

Garver, J., Stratigraphy, depositional setting, and tectonic significance of the clastic cover to the Fidalgo ophiolite, San Juan Islands, Washington, *Can. J. Earth Sci.*, *25*, 417-432, 1986.

Glassley, W. E., J. T. Whetten, D. S. Cowan, and J. A. Vance, Significance of coexisting lawsonite, prehnite, and aragonite, in the San Juan Islands, Washington, *Geology*, *4*, 301-302, 1976.

Jayko, A. S., M. S. Blake, and T. Harms, Attenuation of the Coast Range Ophiolite by extensional faulting and nature of the Coast Range "Thrust", California, *Tectonics*, *6*, 475-488, 1987.

Johnson, S. Y., Stratigraphy, age, and paleogeography of the Eocene Chuckanut formation, northwest Washington, *Can. J. Earth Sci.*, *21*, 92-106, 1984.

Lister, G. S., and P. F. Williams, The partitioning of deformation in flowing rock masses, *Tectonophysics*, *92*, 1-33, 1983.

Maekawa, H., and E. H. Brown, Kinematic analysis of the San Juan thrust system, Washington: *Geol. Soc. Am. Bull.*, *103*, 1007-1016, 1991.

Malvern, L. E., *Introduction to the Mechanics of a Continuous Medium*, 713 pp., Prentice Hall, Englewood Cliffs, N.J., 1969.

McGroder, M. F., Reconciliation of two-sided thrusting, burial metamorphism, and diachronous uplift in the Cascades of Washington and British Columbia, *Geol. Soc. Am. Bull.*, *26*, 1586-1602, 1991.

McKenzie, D., Finite deformation during fluid flow, *Geophys. J. R. Astron. Soc.*, *58*, 689-715, 1979.

Means, W. D., B. E. Hobbs, G. S. Lister, and P. F. Williams, Vorticity and non-coaxiality in progressive deformations, *J. Struct. Geol.*, *2*, 371-378, 1980.

Misch, P., Bedrock geology of the north Cascades, in *Geological excursions in the Pacific Northwest: Bellingham, WA.*, edited by E.H. Brown and R.C. Ellis, p. 1-62, West. Wash. Univ., Bellingham, Wash., 1977.

Mitra, S., A quantitative study of deformation mechanisms and finite strain in quartzite, *Contrib. Mineral. Petrol.*, *59*, 203-226, 1976.

Norris, R. J., and D. G. Bishop, Deformed conglomerates and textural zones in the Otago schists, South Island, New Zealand, *Tectonophysics*, *174*, 331-349, 1990.

Pacht, J. A., Petrologic evolution and paleogeography of the late Cretaceous Nanaimo Basin, Washington and British Columbia: Implications for Cretaceous tectonics, *Geol. Soc. Am. Bull.*, *95*, 766-788, 1984.

Patterson, M. S., and L. E. Weiss, Symmetry concepts in the structural analysis of deformed rocks, *Geol. Soc. Am. Bull.*, *72*, 841-882, 1961.

Patterson, S. R., and H. Yu, Primary fabric ellipsoids in sandstones: Implications for depositional processes and strain analysis, *J. Struct. Geol.*, *16*, 505-517, 1994.

Pavlis, T. L., and R. L. Bruhn, Deep-seated flow as a mechanism for the uplift of broad forearc ridges and its role in the exposure of high P/T metamorphic terranes, *Tectonics*, *2*, 473-497, 1983.

Platt, J. P., Dynamics of orogenic wedges and the uplift of high-pressure metamorphic rocks, *Geol. Soc. Am. Bull.*, *97*, 1037-1053, 1986.

Platt, J. P., The uplift of high-pressure-low temperature metamorphic rocks, *Philos. Trans. R. Soc. London, Ser. A*, *321*, 87-103, 1987.

Platt, J. P., Exhumation of high pressure metamorphic rocks: A review of concepts and processes, *Terra Nova*, *5*, 119-133, 1993.

Press, W. H., B. P. Flannery, S. A. Teukolsky, and W. T. Vetterling, *Numerical Recipes: The Art of Scientific Computing (FORTRAN Version)*, Cambridge Univ. Press, New York, 1990.

Ramsay, J. G. and M. I. Huber, *The Techniques of Modern Structural Geology: vol. 1, Strain Analysis*, Academic Press, San Diego, Calif., 1983.

Ring, U., and M. T. Brandon, Ductile deformation and mass loss in the Franciscan subduction complex: Implications for exhumation processes in accretionary wedges, in *Exhumational Processes: Normal Faulting, Ductile Flow, and Erosion*, edited by U. Ring et al., *Geol. Soc. Spec. Publ.*, in press, 1999.

Schwartz, S., and B. Stöckhert, Pressure solution in siliciclastic HP-LT metamorphic rocks: Constraints on the state of stress in deep levels of accretionary complexes, *Tectonophysics*, *255*, 203-209, 1996.

Selverstone, J., Petrologic constraints on imbrication, metamorphism, and uplift in the SW Tauern window, Eastern Alps, *Tectonics*, *4*, 687-704, 1985.

Smith, M., Deformational geometry and tectonic significance of a portion of the Chilliwack Group, northwestern Cascades, Washington, *Can. J. Earth Sci.*, *25*, 433-441, 1988.

Tabor, R. W., and W. M. Cady, The structure of the Olympic Mountains, Washington: Analysis of a subduction zone, *U. S. Geol. Surv. Prof. Pap. 1033*, 38 pp., 1978.

Tabor, R. W., R. A. Haugerud, D. B. Booth, and E. H. Brown, Preliminary geologic map of the Mount Baker 30-by 60-minute quadrangle, Washington, *U.S. Geol. Surv. Open File 94-0403*, Boulder Colo., 1994.

Truesdell, C., *The Kinematics of Vorticity*, Indiana Univ. Press, Bloomington, Indiana, 1954.

Twiss, R. J., B. J. Souther, and J. R. Unruh, The effect of block motions on the global seismic moment tensor, and the patterns of seismic P and T, *J. Geophys. Res.*, *98*, 645-674, 1993.

Urai, J., P. Williams, and H. van Roermund, Kinematics of crystal growth in syntectonic fibrous veins, *J. Struct. Geol.*, *13*, 823-836, 1991.

Vance, J. A., Metamorphic aragonite in the prehnite-pumpellyite facies, northwest Washington, *Am. J. Sci.*, *266*, 299-315, 1968.

Vance, J. A., Bedrock geology of San Juan County, in *Geology and Water Resources of the San Juan Islands*, edited by R. H. Russell, Water Supply Bulletin, Wash. Dep. Ecol., *46*, 3-19, 1975.

Wallis, S.R., Vorticity analysis in a metachert from the Sanbagawa Belt, SW Japan, *J. Struct. Geol.*, *14*, 271-280, 1992.

Wallis, S.R., Vorticity analysis and recognition of ductile extension in the Sanbagawa Belt, SW Japan, *J. Struct. Geol.*, *17*, 1077-1093, 1995.

Whetten, J. T.,. The geology of the southeastern San Juan Islands, in *Geology and Water Resources of the San Juan Islands*, edited by R. H. Russell, Water Supply Bulletin, Wash. Dep. Ecol., *46*. 341-357, 1975.

Williams, P. F., Development of metamorphic layering and cleavage in low grade metamorphic rocks at Bermagui, Australia, *Am. J. Sci.*, *272*, 1-47, 1972.

J. G. Feehan and M. T. Brandon, Department of Geology and Geophysics, Yale University, P.O. Box 208109, 210 Whitney Ave., New Haven, CT 06520-8109. (email: mark.brandon@yale.edu)

(Received November 18, 1997; revised August 25, 1998; accepted October 5, 1998.)